



Review

Unique optical properties and applications of hollow gold nanospheres (HGNS)



Staci Adams, Jin Z. Zhang*

Department of Chemistry and Biochemistry, University of California, Santa Cruz, CA 95064, USA

Contents

1. Introduction.....	19
1.1. Localized surface plasmon resonance (LSPR) and Mie theory.....	19
1.2. Metal nanostructures.....	19
2. Synthesis of hollow gold nanospheres (HGNS).....	20
2.1. Amorphous template mediated approaches to synthesis.....	20
2.2. Galvanic replacement.....	20
2.3. Tuning the LSPR of HGNS.....	21
2.3.1. Tuning LSPR to the NIR.....	21
2.3.2. Tuning the LSPR with temperature.....	21
2.4. Optimizing reproducibility of NIR absorbing HGNS.....	22
2.4.1. NIR reproducibility using poly (vinylpyrrolidone) (PVP).....	22
2.4.2. Non-polymer NIR reproducibility.....	22
3. Energy conversion, heat generation, and energy transfer.....	23
3.1. Electron dynamics.....	23
3.2. The influence of laser mode and power.....	24
4. Photothermal therapies.....	26
4.1. Photothermal ablation (PTA) therapy.....	26
4.2. PTA with HGNS.....	27
4.3. Multi-modal treatments.....	27
4.3.1. Cancer drug delivery plus PTA.....	28
4.3.2. Photothermal transfection.....	28
5. Surface enhanced Raman scattering (SERS) and electromagnetic (EM) field enhancement.....	29
5.1. Plasmon coupling in aggregates for SERS.....	29
5.2. First hyperpolarizabilities (β).....	30
5.3. SERS immunoassays.....	31
5.4. SERS nanotags.....	32
6. Imaging.....	32
7. Concluding remarks.....	33
Acknowledgments.....	33
References.....	33

ARTICLE INFO

Article history:

Received 26 November 2015

Received in revised form 28 January 2016

Accepted 31 January 2016

Available online 16 March 2016

ABSTRACT

The field of plasmonics is driven by the investigation of the interaction between the electromagnetic (EM) field (light) and metal nanostructures. In particular, noble metal nanoparticles have been studied extensively due to their interesting surface plasmon resonance (SPR) properties and related applications. Tuning of the SPR position in energy is possible through synthetic variation in size, shape, aspect ratio, the

Abbreviations: HGN and HAUNS, hollow gold nanosphere; EM, electromagnetic; SPR, surface plasmon resonance; LSPR, localized surface plasmon resonance; SERS, surface enhanced Raman scattering; PTT, photothermal therapy; PTA, photothermal ablation therapy; QD, quantum dot; NP, nanoparticle; FWHM, full-width-half-maximum; HAADF-STEM, high angle annular dark field scanning transmission electron microscopy; S/V, surface to volume ratio; TEM, transmission electron microscopy; LOD, limit of detection; NIRF, near infrared fluorescence; PET, positron emission tomography; OAT, optical acoustic tomography; PAT, photo acoustic tomography; MRI, magnetic resonance imaging; CW, continuous wave; PW, pulsed wave; ELISA, enzyme linked immunosorbent assay; ND, neutral density; DOX, doxorubicin; NIR, near infrared; UV-vis, ultraviolet-visible.

* Corresponding author. Tel.: +831 459 3776.

E-mail address: zhang@ucsc.edu (J.Z. Zhang).<http://dx.doi.org/10.1016/j.ccr.2016.01.014>

0010-8545/© 2016 Elsevier B.V. All rights reserved.

Keywords:

Hollow gold nanospheres
 Plasmonics
 Photothermal therapies
 Surface enhanced Raman scattering (SERS)
 Hot electron dynamics
 Energy conversion

dielectric constant of the surrounding media, surface morphology and whether particles are aggregated. One unique metal structure capable of meeting a wide range of criteria for multiple applications calling for enhanced EM field is the hollow gold nanosphere (HGN). HGNS have hollow solvent filled dielectric cores and polycrystalline gold shells that, due to the two surfaces or interfaces, can generate enhanced EM field. They possess a unique combination of properties that include small size (20–125 nm), large surface to volume (S/V) ratios, spherical shape, narrow and tunable SPR (~520–1000 nm), and biocompatibility. Their surfaces can also be easily functionalized to target and deliver biomolecules and are resistant to photobleaching. Additionally their scattering and absorption cross-sections can be tailored, making them excellent candidates for a variety of applications including surface enhanced Raman scattering (SERS), sensing, imaging, drug delivery, site specific silencing, and photothermal therapies (PTTs). This review will provide a perspective on the continued investigation of the plasmonic properties associated with HGNS and how these properties can be refined and harnessed for emerging applications.

© 2016 Elsevier B.V. All rights reserved.

1. Introduction

1.1. Localized surface plasmon resonance (LSPR) and Mie theory

Localized surface plasmon resonance (LSPR), one of the unique properties associated with noble metal nanoparticles, has been studied extensively [1–12]. When metal nanoparticles are exposed to light on resonance with their absorption wavelength, a collective oscillation of electrons in the conduction band takes place [13,14]. This creates a charge separation with respect to the lattice [2,15]. The confined conduction band electrons in the small particle volume then begin to move in phase with the radiation plane wave excitation, creating a coherent electromagnetic (EM) response which strengthens both the near field energy and the optical extinction associated with the nanoparticle surface [16,17]. The optical extinction, or maximum intensity of the oscillation frequency, is composed of both scattering (elastic and radiative) and absorption (inelastic and non-radiative) efficiencies [14,17]. The coherent oscillatory response of a dipole induced noble metal nanoparticle conduction band electrons on resonance with an incident light at a specific frequency is illustrated schematically in Fig. 1.

The bandwidth, or full width half maximum (FWHM) of the absorption peak is inversely proportional to the coherence time, or period that the oscillating electrons stay in-phase before damping [14,18,19]. The effective radiative damping of a dipolar plasmon will be proportional to the nanoparticle volume where smaller nanoparticles will have intrinsic, or thermoelastic, damping as their dominant decay mechanism [9,20]. For nanoparticles with diameters greater than 50 nm radiative damping will dominate [16,21].

Faraday was the first to propose that the brilliant colors observed in gold doped stain glass and colloidal solutions illuminated by visible light were the result of “finely divided” minute particulates of bulk gold [22]. Later, Mie developed the relationship between light and noble metal nanoparticles, which generates the LSPR [23]. Using Maxwell’s equations, he modeled the interaction of spherical nanoparticles with a diameter much smaller than that of the resonant incident radiation and determined the scattering of their EM waves in terms of an infinite series of multipolar partial wave contributions [24,25]. Mie established that under these conditions nanoparticles will experience a spatially constant EM field with a time dependent phase known as the quasistatic limit and that the dipolar mode with polarizability α will dominate the LSPR of a spherical metal nanoparticle [26,27]. This polarizability can be defined by:

$$\alpha = 3\varepsilon_0 V \left(\frac{\varepsilon - \varepsilon_m}{\varepsilon_r + 2\varepsilon_m} \right) \quad (1)$$

where, ε_0 is the vacuum permittivity, V is the particle volume and ε_m is the dielectric constant of the surrounding medium [1].

According to Mie theory, the extinction cross-section for a given nanoparticle can be determined by Eq. (2) and the absorption contribution can be evaluated with Eq. (3):

$$C_{\text{ext}} = \frac{24\pi 2R^3 \varepsilon_m^{3/2}}{\lambda} \frac{\varepsilon_i}{(\varepsilon_r + 2\varepsilon_m)2 + \varepsilon_i^2} \quad (2)$$

$$C_{\text{abs}} = \frac{18\pi f \varepsilon_m^{3/2}}{\lambda} \frac{\varepsilon_i}{(2\varepsilon_m + \varepsilon_r)^2 + \varepsilon_i^2} \quad (3)$$

where, R is the particle radius, λ is the wavelength of light, f is the fraction of the core volume, ε_m is the dielectric constant of the surrounding medium and ε_r and ε_i are the real and imaginary components of the complex dielectric constant of the nanoparticle [28,29]. The scattering contribution can then be calculated by subtracting the absorption coefficient from the total extinction value. Here the real part of the dielectric constant determines the position of the wavelength while the bandwidth, or time spent dephasing, is determined by the imaginary component [18,30–33]. In general, for smaller nanoparticles, <40 nm, the optical extinction is dominated by absorption whereas scattering contributions increase as the diameter of the nanoparticle grows [21,33,34].

1.2. Metal nanostructures

The use of metal nanostructures in many applications including bio-diagnostics, bio-delivery and photothermal therapies depends almost entirely upon their ability to harvest light and generate strong EM fields. Tuning of the LSPR properties can be achieved through synthesis by exploiting differences in nanoparticle size,

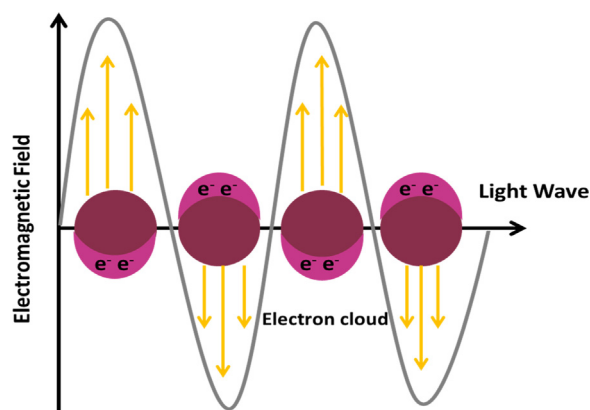


Fig. 1. The coherent oscillatory response of the dipole induced noble metal nanoparticle conduction band electrons on resonance with incident frequency of light.

geometry, surface morphology, aggregation, aspect ratio, and the dielectric constant of the surrounding media [15,33,35–45]. Since each application relies on a specific set of conditions for optimized efficiency, the structural parameters of the nanoparticles employed for use must be tailored accordingly.

In general, overlap between nanoparticle's LSPR and the incident excitation wavelength of light should be maximized to ensure the greatest absorption of light and thereby amplification of EM field. This can be achieved largely through geometric design [2,16,17,46–51]. While many structures exhibit suitable enhancement of their EM field in response to incident light, their lack of symmetry results in multiple resonances due to non-degenerate electronic transitions [52,53]. This means for a given light wavelength, not all the LSPR transitions will be excited or on resonance.

For example, nanorods have two resonant peaks, a transverse band and another corresponding to the longitudinal mode of the structure [35,54,55]. Aggregates, which are random assemblies of nanoparticles, can have multiple resonances depending on their size and shape, especially when the interaction between particles is strong [18,53,56,57]. This is also true for triangles, stars, cubes and cages [37,42,46,48,58].

Nanoshells are another type of metal nanostructures with interesting optical properties useful for various applications [59–63]. These structures, which are typically made of spherical silica cores surrounded by a layer of noble metal aggregates, have variation in size, shape and surface morphology due to the random nature of aggregation [64,65]. The polydispersity found within a given ensemble of shells will lead to a broadening of the extinction line width [66]. This results in reduced overlap with incident light and lower efficiency for processes such as photothermal conversion.

Since skin, tissue and blood are most readily penetrated by NIR light, nanoparticles employed in biological applications should have strong absorption in this region [5,67,68]. Structures should ideally be spherical with diameters in the range of 20–100 nm [69–72]. This promotes both optimal cell penetration and bio-clearance [70,71,73]. Additionally, nanomaterials must be stable to photodegradation, biocompatible and capable of conjugating easily to biomolecules [53,60,74]. However, most commonly used structures lack one or more of these requirements, and their use in many bio-applications still needs to be optimized.

One particularly attractive class of nanoparticles is the hollow gold nanosphere (HGN). HGNS are comprised of a hollow, solvent filled dielectric core and a polycrystalline gold shell [66,75–77]. Both the core width and shell thickness can be tuned through synthesis to produce a range of overall diameters (20–125 nm) and aspect ratios. As a two-interface system HGNS have enhanced LSPR which is the result of strong coupling in the near-field between the plasmon modes of the inner cavity surface and the outer surface [8,9,29,38]. This coupling leads to the hybridization of the two individual plasmon modes where the plasmons interact electrostatically with one another in the same manner as a coupled harmonic oscillator [8,9]. The strength of this coupling is proportional to the aspect ratio of the nanoparticle [8]. As the shell becomes thinner and the aspect ratio increases, the interaction between the cavity and the shell plasmons is amplified producing an enhancement of the EM field associated with the HGNS.

HGNS are also biocompatible, stable to photodegradation and can be easily functionalized for use in bio-targeting and bio-delivery [53,60,78–80]. These particles also possess large surface to volume (S/V) ratios, tunable plasmon resonance, pinholes that act as hot spots to further intensify EM surface energy and, as hollow structures, are known to be more sensitive to the refractive index of their surroundings than their solid counterparts [15,66,81–84]. Additionally, their scattering and absorption cross-sections can be adjusted through synthesis to maximize efficiency for specific applications, and since the first hyperpolarizabilities (β) of hollow

nanoparticles are much larger than those of solid NPs having the same size, HGNS are excellent candidates for any application involving non-linear optics [85,86].

This review will focus on the current understanding of the plasmonic properties of HGNS and their various emerging applications. The synthetic development of HGNS will also be explored with an emphasis on how differences in synthetic parameters results in nanoparticles with various sizes, aspect ratios, surface morphologies and scattering and absorption efficiencies. Additionally, the expanding use of HGNS in a variety of bio-medical applications including photothermal therapies, drug delivery, imaging and sensing will be described.

2. Synthesis of hollow gold nanospheres (HGNS)

2.1. Amorphous template mediated approaches to synthesis

Early hollow structures were typically made from amorphous materials like ceramics or polymeric substances where the sacrificial core was dissolved out chemically [87–89]. However, dissolvable template mediated approaches typically produce structures that are larger than 100 nm, making them undesirable for most biological applications where particles should be in the 20–100 nm size regime [72,74,80]. Additionally, removal of templates generally involves the introduction of impurities and adds an additional step in the synthetic process which increases both the difficulty of nanoparticle preparation and the time involved for synthesis [90–92].

It has been reported that hollow gold nanospheres have been produced in this way [93–95]. In one case HGNS were synthesized by deposition of gold on to a template that was then exposed to tetrahydrofuran as a chemical leaching agent [94]. In another, a Si template that was functionalized with 3-aminopropyltrimethoxysilane (APTMS) to facilitate gold shell deposition was subjected to hydrofluoric acid (HF) etching in order to generate HGNS [95]. Chah et al. reported the synthesis of both 50 and 100 nm gold hollow microspheres from dissolvable ceramic hollow sphere templates [93].

2.2. Galvanic replacement

A less complicated approach for synthesizing hollow structures is galvanic replacement. Galvanic replacement is an electrochemical redox reaction where the oxidation of one metal, the sacrificial template, is generated by contact in solution with another metal having a higher reduction potential [96–99]. The template being oxidized, possessing the lower reduction potential and higher rate of diffusion, loses electrons and the metal being reduced gains electrons. Oxidation is initiated on the crystal lattice plane of the sacrificial template exhibiting the highest surface energy [84,100–102]. Small pinholes, or Kirkendall voids, are formed as a result of this oxidation [103,104]. It is the diffusion of the template through an increasing number of voids that generates the hollow structure [105].

In the mid 20th century, Kirkendall established, in an alloying reaction, using copper and zinc in brass, that atomic diffusion between an interacting atomic pair occurs not through the direct interchange of atoms, but by vacancy exchange generated by the oxidation of one metal [105]. Simple steady state diffusion governed by Fick's first law and the Gibbs–Thomson effect, which states that diffusion is driven by differences in the chemical potential and equilibrium concentrations of interacting atoms, govern the thermodynamics of the reaction [97,104,106,107].

Recently Goris et al. used high angle annular dark field scanning transmission electron microscopy (HAADF-STEM) tomography to

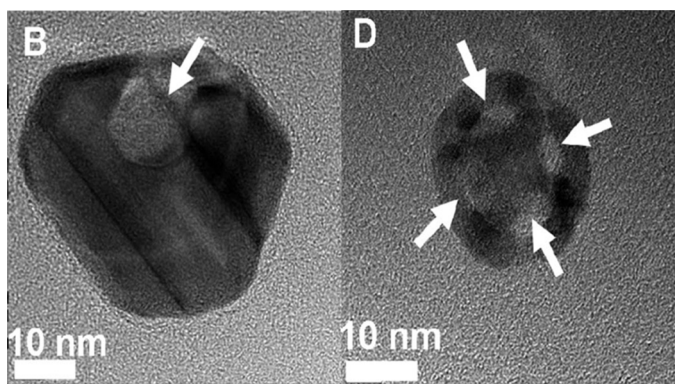


Fig. 2. TEM images of HGN synthesized after reacting the Ag NPs with (B) 0.75 ml and (D) 1.45 ml of aqueous HAuCl₄ solution. The arrow in B indicates the formation of holes on the surface and the hollow nanostructure in the interior. The arrows in D indicate the pinholes and the porous surface (Reprinted with permission from reference [84], Copyright 2009).

investigate pinhole formation during a galvanic replacement reaction between Ag nanocubes and chloroauric acid (HAuCl₄) [102]. As gold salt was added to the Ag nanocubes, circular holes appeared on the highest energy [111] plane. Previously Wu et al. used TEM to demonstrate the formation of pinholes on the surface of Ag nanocubes involved in a galvanic replacement reaction with HAuCl₄ and two of these images can be seen in Fig. 2 [84]. However, Gori's work was the first experimental evidence that pinholes are initiated on only one facet of the crystal lattice and that the reduced metal in a galvanic replacement reaction is deposited first around these pinholes [102].

2.3. Tuning the LSPR of HGNs

The first HGNs produced through galvanic replacement were synthesized by Xia et al. [108]. In this work, the authors utilized the fact that the reduction potential of the AuCl₄⁻/Au pair is greater than that of the Ag⁺/Ag and that silver suspended in solution can be readily oxidized by HAuCl₄ to produce a hollow gold nanostructure. The resultant HGNs had a 50 nm diameter, a 6.6 nm shell, an SPR of 634 nm and a full width half maximum (FWHM) of 227 nm [108].

In 2005 Liang et al. also used galvanic replacement to produce HGNs, but instead of using silver as a sacrificial template, used cobalt (Co²⁺/Co⁰ -0.377 V vs. SHE) and gold (AuCl₄⁻/Au⁰ 0.935 V vs. SHE) as the redox pair [75]. In this case the facet energies of the hexagonal close packed (HCP) structure of the cobalt template are known to increase 0001 < 10-10 < 10-11 < 11-20 < 10-12 < 11-21 with respective energies of 131, 140, 149, 155, 156, 163 (meV/Å²) [109]. This means that the oxidation and generation of Kirkendall voids were initiated on the [11-21] plane of the cobalt lattice.

By varying the stoichiometric ratio of HAuCl₄ to cobalt, Liang et al. was able to red shift the LSPR of the HGNs from ~520 nm, where solid gold absorbs, to ~628 nm [75]. The key to controlling the nucleation and growth of the cobalt template was through the use of excess reducing agent (sodium borohydride), which had been previously reported by Liseiecki et al. [110]. The red shift in absorption was attributed to differences in shell thickness which were controlled by the addition of varying stoichiometric ratios of gold to cobalt with smaller additions of gold resulting in thinner shells with enhanced absorption at longer wavelengths [75].

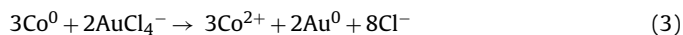
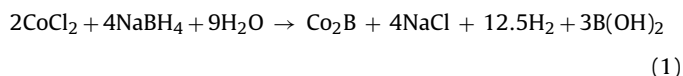
2.3.1. Tuning LSPR to the NIR

Expanding on the work of Liang et al., Schwartzberg et al. used the same redox pair [cobalt and gold] to tune the LSPR of HGNs across the entire visible spectrum and out to the NIR [66]. It was recognized that control of the cobalt sacrificial template diameter

was the key to producing larger HGNs with red shifted absorptions. This could be achieved by varying the stoichiometric ratio of the CoCl₂ precursor and capping agent as described by Kobayashi et al. who reported that as the concentration of the capping agent was reduced, the size of the cobalt nanoparticle diameter increased [111]. Since the concentration of capping agent not only stabilizes the cobalt nanoparticle seed-mediated growth but also affects the number of nucleation sites generated post-reduction, lower concentrations of capping agent lead to a smaller number of larger seed nuclei being formed [112]. This resulted in cobalt nanoparticles, and therefore HGNs, with larger diameters [66].

The kinetics related to the addition of the borohydride reducing agent was also investigated [66]. In order to obtain monodispersed particles, it is necessary to increase the nucleation rate so that after the initial nucleation burst no more seeds are formed [113]. When the reduction kinetics were slowed, seeds that formed initially had more time to grow, while those seeds formed later had less time to grow [66]. This resulted in an undesirable polydisperse population. In contrast, increasing the rate at which the reducing agent was added to the reaction precursors resulted in an even reduction of the Co salt and an equal growth period for all the seeds [66]. This enhanced the homogeneity of the size distribution of the ensemble.

The HGN synthetic reaction proceeds according to the following proposed mechanism: [75,114]



In the first step, a Co₂B species is formed following the reduction of the CoCl₂ salt by NaBH₄. In the absence of oxygen, only this species is formed [114]. However, in the presence of oxygen, the boron atom is oxidized to B₂O₃ as the cobalt atom is reduced to elemental Co (step 2) [114]. In the process of reduction, the NaBH₄ overcomes an energy barrier through supersaturation and creates a nucleation burst of cobalt seeds [115]. Then through diffusional capture of atoms in solution, seeds coalesce in to primary clusters that then aggregate to form larger spherical particles [115].

In general, particle growth kinetics are governed by differences in chemical equilibrium at the solid-liquid interface, the total free energy of the nanoparticle (sum of surface free energy and bulk free energy) and by the concentration of reagents available to the growing particle [113,116,117]. In the case of HGNs, there needs to be some oxygen to facilitate the reduction of cobalt salt and growth of cobalt nanoparticles, but if too much oxygen is present the cobalt will oxidize to form cobalt oxide [114]. Once the cobalt template has reached a fixed diameter, galvanic replacement (step 3) is initiated. In this step elemental cobalt is oxidized back to a salt and the HAuCl₄ species is reduced to a polycrystalline shell [66,75].

The LSPR of the HGNs can be tuned by changing the aspect ratio, or the ratio between the core and shell diameter. As the aspect ratio increases, the HGNs will absorb longer wavelengths of light [66,83,118,119]. For a fixed core diameter, decreasing the volume of the gold salt delivered produces a thinner shell and red-shifted absorption whereas a constant shell thickness and a decreasing core diameter produce blue-shifted SPR [66,83,120,121]. Fig. 3 shows the UV-vis absorption spectra of nine HGN samples with varying diameters and shell thicknesses. As the ratio of the core diameter to the shell thickness increases the extinction peak red-shifts [66].

2.3.2. Tuning the LSPR with temperature

Another means of tuning the size and LSPR of HGNs is through temperature. Pu et al. (Pu and Song et al., unpublished) found that

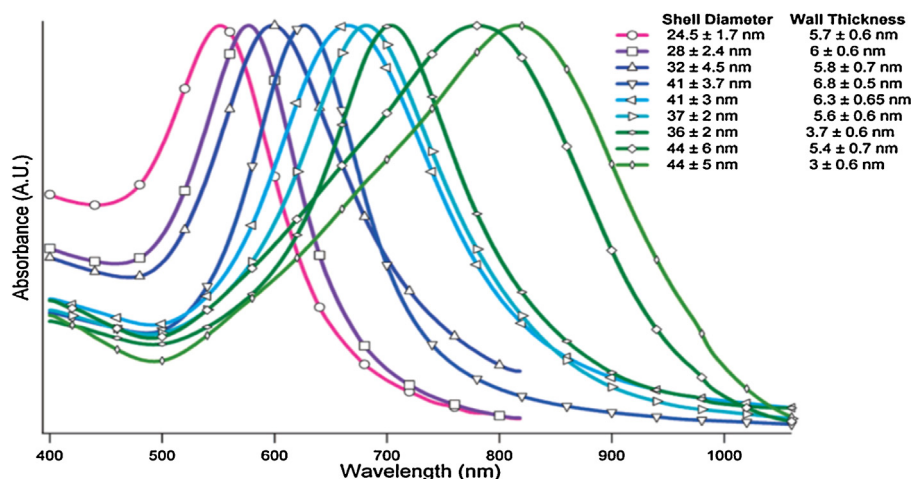


Fig. 3. UV-vis absorption spectra of nine HGN samples with varying diameters and shell thicknesses. (Reprinted with permission from reference [66]. Copyright 2006).

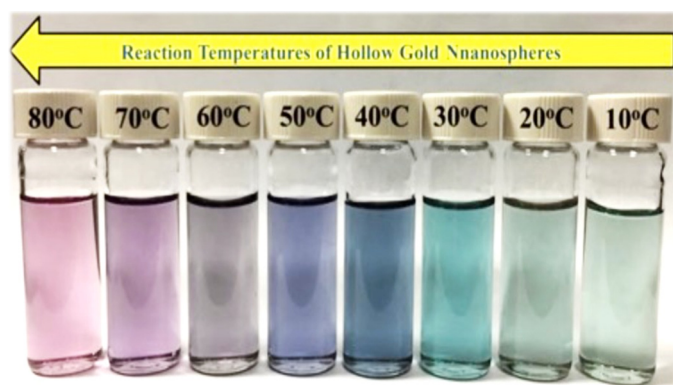


Fig. 4. HGN colloidal solutions prepared at eight temperatures. As the temperature of the reaction is increased the resulting HGN absorption is blue-shifted resulting in a difference in perceived color due to increased scattering contributions to the total extinction. (Reprinted with permission from Pu and Song et al., 2015 unpublished).

by altering the temperature during the cobalt reduction step, control could be gained over the final template diameter which alters the optical extinction of the resulting HGN. It has been reported previously that HGNS synthesized by an alternative synthetic method have absorption wavelengths that blue shift as the reaction temperature is increased [122]. Pu and Song also observed this trend (Pu and Song et al., unpublished).

In their work, Pu et al. found that as the reaction temperature was raised in ten degree increments from 10 °C to 80 °C, the overall diameter of the HGN decreased from 150 nm to 30 nm and the SPR was blue-shifted from 855 nm to 565 nm (Pu and Song et al., unpublished) Fig. 4 is a photograph of HGNS synthesized at various temperatures. Lower temperatures produce larger HGNS that scatter more light and appear blue or green, while higher temperatures produce HGNS that appear purple or red. It was determined that temperature was directly proportional to the size of the cobalt sacrificial template produced, with higher temperatures producing smaller Co core (Pu and Song et al., unpublished) This is believed to be the result of the thermodynamic influence on nucleation which is controlled in part through the increase in surface free energy associated with the increase in reaction temperature [123,124].

2.4. Optimizing reproducibility of NIR absorbing HGNS

The ability to tune the SPR of HGNS was significant and allowed for their use in a variety of applications like photothermal ablation therapy (PTA), surface enhanced Raman scattering (SERS) and

imaging that require nanoparticles with specific colors, sizes and absorptions wavelengths. However, the ability to generate NIR absorbing HGNS for biological applications including photothermal therapies still needed to be improved.

2.4.1. NIR reproducibility using poly (vinylpyrrolidone) (PVP)

The first to address enhancing HGN reproducibility in the NIR was Preciado-Flores et al. who employed the integration of poly (vinylpyrrolidone) (PVP) during the reduction step to generate large cobalt core diameters with thin Au shells [76]. PVP has been shown to coordinate effectively with cobalt and is an excellent colloidal NP stabilizing agent [125,126]. The growth of red-shifted HGNS was achieved through the carbonyl-induced stabilization of the cobalt NPs by the PVP [76]. This strong interaction was determined to be the key in slowing down Au nucleation which resulted in thinner shell diameters, increased aspect ratio and redder wavelengths of absorption [76].

However, the addition of PVP produced variation in both the core diameter and shell thickness. Additionally, shells had spikey, star-shaped morphologies believed to result from a lack of porosity caused by the presence of PVP, which prevents efficient diffusion [76]. It was also observed that the addition of PVP lead to organized backbone-like structures in which the gold shell formed preferentially along the traverse axis of the particle chain due to the dense solvating shell of the polymer [76].

These structures showed broadening of the total extinction indicative of a polydispersed ensemble [56]. While these morphologies and extended spatial arrangements may benefit an application like SERS, where aggregation and particle alignment generate hot spots which enhance scattering, a more monodispersed population is desired for applications like photothermal therapies that require enhanced resonance with incident laser light for greater efficiency of heat generation and transfer [127].

Currently, the Zhang Lab is investigating how surface morphology affects the performance of HGNS. Through pH control during galvanic replacement, it has been found that the surface morphology of the gold shell can be altered from smooth to studded to anemone-like in a systematic manner. The absorption and scattering ratios, coherent vibrational oscillations after photoexcitation, and the relation to heat generation are currently being assessed.

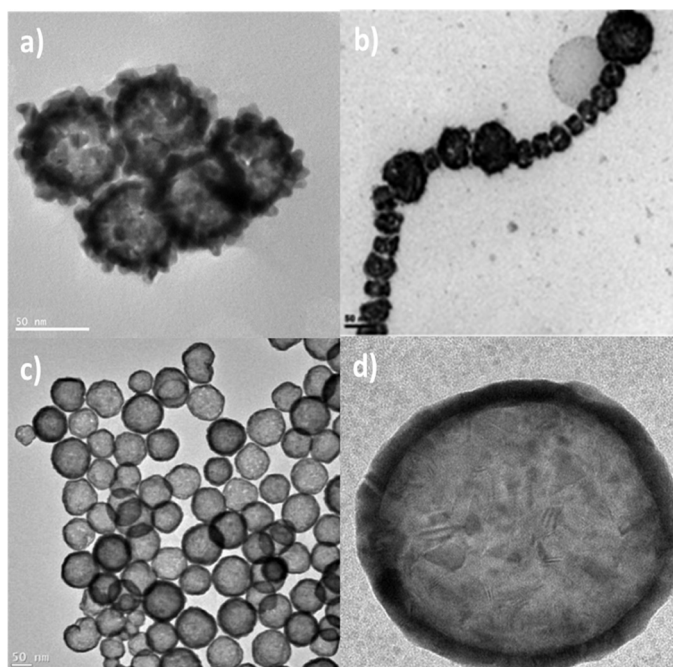


Fig. 5. HGNs synthesized with PVP produce: (a) spikey star shaped surface morphology and (b) backbone like chain structures. HGNs synthesized in the absence of polymers are: (c) more homogeneous with respect to size and surface morphology and d) have smoother and more uniform shells. (a) reprinted with permission from reference [77]. Copyright 2014, (b) reprinted with permission from reference [76]. Copyright 2010, (c and d) reprinted with permission Adams et al. unpublished.

2.4.2. Non-polymer NIR reproducibility

Another effort focused on improving the synthetic reproducibility of NIR absorbing HGNs has been reported [77]. In this work an emphasis was placed on not only gaining control of the cobalt NP growth in order to maximize the size of the template but also on separating the nucleation and growth phases of the growing Co NPs. This was achieved by optimizing reagent concentrations, and evaluating the kinetics of the cobalt nanoparticle growth [77].

In order to obtain large, monodispersed particles, it is necessary to increase the rate of nucleation so that after the initial seed burst no additional nuclei are formed [116,117]. This ensures an early saturation point is achieved and precursors will only deposit on existing nuclei [113]. It was found that the addition of citric acid, which acts as a scavenging agent for excess borohydride, shortened the hydrolysis time leading to a uniform growth period for the evenly reduced cobalt seeds [77].

It is known that cobalt NPs are highly sensitive to oxidation and that prevention of oxidation leads to nanoparticles which are more uniform in size and surface morphology [114,128,129]. For this reason a time course study to determine the optimal incubation period between the reduction step and galvanic replacement step was used to determine if the reaction time could be shortened to prevent potential Co oxidation [77].

Previous reports allowed the cobalt NPs to grow for 45–60 min [66,76]. However, cobalt NPs that were allowed to grow this long succumbed to oxidation and suffered degradation of their surfaces [77]. This produced significant broadening of the absorption full-width-half-maximum (FWHM) indicative of diversity within the ensemble. Stopping the cobalt growth at 10 min produced the narrowest NIR extinction bandwidth and the most monodispersed ensemble [77].

Overall, this synthetic optimization allowed highly reproducible, uniform, NIR absorbing HGNs to be generated without the use of polymers [77]. Furthermore, the reaction time was reduced significantly from ~2.5 h to ~25 min. Fig. 5 shows electron

microscopy images of HGNs synthesized with and without polymers. It can be seen that HGNs synthesized with PVP produce spikey, uneven surface morphologies and align themselves in chain-like formations while HGNs prepared without the addition of polymers are more uniform in size and exhibit smooth surface morphologies [77].

3. Energy conversion, heat generation, and energy transfer

The ability of a nanoparticle to generate and transfer sufficient heat is critical in applications where temperature is either applied to trigger drug release, facilitate gene silencing or generate hyperthermia in the treatment of cancer. In order to fully understand and optimize the plasmonic response of a nanoparticle, electron dynamics must be studied. Femtosecond time resolved transient absorption laser spectroscopy is frequently employed to evaluate how differences in aspect ratio, size, shell thickness, aggregation, and the dielectric constant of the surrounding medium influence energetic conversion and transfer [16,31,35,130–138]. However, due to the complex interplay of parameters, optimizing a structure for SPR absorption in the NIR is not the same as optimizing a nanoparticle for maximal generation and transfer of heat.

Conversion of externally applied light into thermal energy and the transfer of heat from irradiated noble metal nanoparticles to their surroundings occurs through a multi-step process. Following excitation, electronic relaxation is initiated through electron–electron scattering which occurs within a few hundred femtoseconds [18,134,139]. This is followed by the transfer of the thermalized hot electron gas to the nanoparticle lattice (electron–phonon coupling) where a quasi-equilibrium state is reached in ~1 ps [9,35,140–143]. The energy exchange between the hot electrons and phonons results in hot phonons and can be described by the two-temperature model which is used to determine the electron–phonon coupling constant g [144–146]. The final step involves relaxation of phonons on the time scale of hundreds of ps, which leads to energy transfer to the surroundings (phonon–phonon interactions) like a solid matrix or solvent molecules [2,57,134,145–150].

3.1. Electron dynamics

Knappenberger et al. found the electron–electron scattering lifetimes for 48 nm HGNs with 7 nm shells (150 ± 70 fs) were shorter than those of aggregated HGNs (300 ± 50 fs) [134]. A blue-shifted absorption for HGN aggregates was also observed. This can be seen in Fig. 6 and is attributed to electron “spill-out” or confinement in the nanoclusters and the delocalization of electrons over multiple particles [134]. Additionally, Fig. 6 shows the femtosecond transient absorption spectra of both, HGNs and HGN aggregates. The aggregated sample has two negative amplitudes, one corresponding to the 605 nm HGN differential SPR and a second at 550 nm corresponding to a new resonance resulting from particle–particle interactions within the aggregate [134].

In this work the authors also determined the electron–phonon coupling rates for isolated HGNs and solid Au NPs [134]. They found the electron–phonon coupling rate for isolated HGNs to be faster (0.59 ± 0.08 ps) than that of 50 nm solid Au NPs (1.08 ± 0.08 ps). The corresponding g values were calculated for HGN aggregates ($6.6 \times 10^{16} \text{ W m}^{-3} \text{ K}^{-1}$) and solid Au spheres ($2.7 \times 10^{16} \text{ W m}^{-3} \text{ K}^{-1}$) using the two-temperature model [134]. The larger electron–phonon coupling constant observed for the HGN aggregates is correlated to rapid electron cooling and greater lattice heating efficiency [136,151]. Faster electronic relaxation is attributed to greater electron–phonon coupling [141].

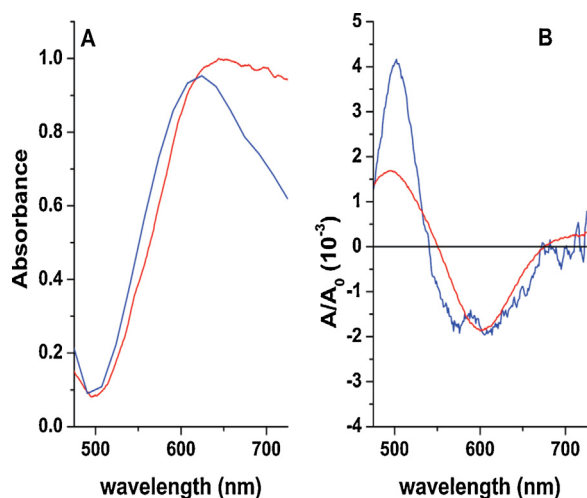


Fig. 6. (A) Absorption spectra of colloidal HGNs (red) and HGN aggregates (blue). A clear blue shift in the aggregate spectrum is apparent. (B) Femtosecond transient absorption spectra of HGNs (red) and HGN aggregates (blue). The nanospheres are excited with 405 nm (500 nJ/pulse) and probed at 500 fs time delay with a white-light continuum probe. The aggregate spectrum contains two negative amplitude (bleach) features centered at 550 and 605 nm. (Reprinted with permission from reference [134]. Copyright 2009).

The transfer of energy between hot electrons and the nanoparticles can be observed as coherent vibrational oscillations which are indicative of the breathing modes of the nanoparticle lattice [57,152,153]. The amplitude of the coherent oscillations of HGNs can be correlated to aspect ratio since amplitude is inversely proportional to the electron–phonon coupling constant g [153,154]. When Dowgiallo et al. investigated HGNs with aspect ratios of 0.38 and 0.75 using femtosecond laser spectroscopy it was found that the lower aspect HGNs had a modulated signal intensity that was only 65% of the amplitude observed for the higher aspect ratio HGNs [155]. These aspect ratios correlated to coupling constants of $\sim 3 \times 10^{16}$ and $\sim 7 \times 10^{16} \text{ W m}^{-3} \text{ k}^{-1}$, respectively. Additionally, the higher aspect ratio HGNs exhibited a decrease in oscillation frequency which was in agreement with a previous report describing a linear decrease of the oscillation frequency for increasing aspect ratio [156]. Fig. 7 shows the Fourier transformation of transient absorption time-domain data for five separate HGN samples with aspect ratios ranging from 0.38–0.75 and particle diameters spanning 10–40 nm [155].

The other interesting result observed by Dowgiallo et al. was that two types of coherent acoustic vibrations could be observed for HGNs depending on their overall diameter and aspect ratio [155]. Low aspect ratio HGNs were observed to have Fourier transformed transient bleach recovery intensity periodic frequencies that were sinusoidal in nature [155]. This is attributed to a direct launching mechanism previously observed in solid Au nanoparticles, which also have sinusoidal frequencies, and is believed to be the result of deformation caused by the incident laser pulse [132,154]. High aspect ratio HGNs had a π phase shift and required a cosine function to fit the data indicative of excitation via an indirect mechanism [132,153]. It was also determined that high aspect ratio HGNs have slower vibrations than low aspect ratio HGNs due to polycrystallinity of the shell lattice and efficient cooling processes and that there is an inversely proportional linear relationship between vibrational frequency and aspect ratio [155].

Ultrafast pump-probe laser spectroscopy has also been used to evaluate the coherent vibrational oscillations of HGNs with average core diameters between 16.4 and 18.8 nm with shell thicknesses between 3.4 and 4.7 nm [136]. All HGNs in the study were found to have heavily damped radial breathing mode oscillations with

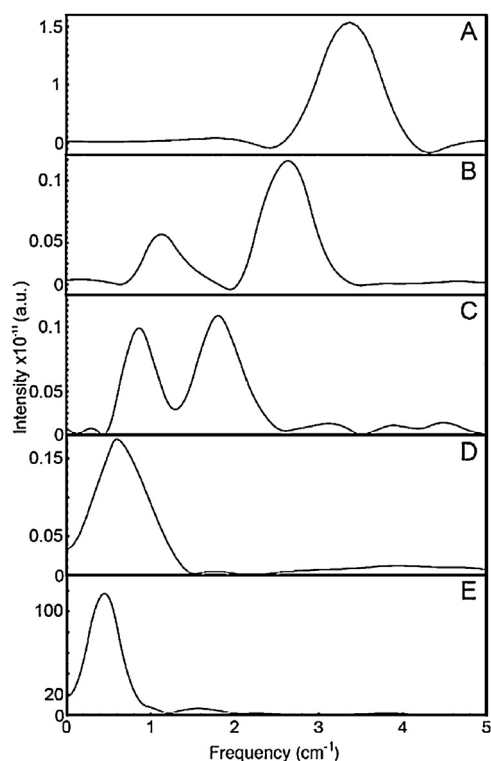


Fig. 7. Fourier transformation of transient absorption time-domain data for a series of HGNs. (A) outer radius (OR) = 10 nm and aspect ratio (AR) = 0.38, (B) OR = 15 nm and AR = 0.46, (C) OR = 25 nm and AR = 0.60, (D) OR = 28 nm and AR = 0.67, and (E) OR = 40 nm and AR = 0.75. (Reprinted with permission from reference [155]. Copyright 2011).

periods ranging from 28 to 33 ps. Theoretical calculations were used to determine how shell thickness and particle radius impacted the fundamental breathing mode of HGNs. For an HGN with a constant overall radius of 8.9 nm and a shell thickness that increased from 1–7 nm, T_{osc} decreased from 13.6 to 6.6 ps [136]. In the case of the HGN with the 7 nm shell, T_{osc} is nearly identical to the experimental T_{osc} of ~ 5.8 ps reported for a solid Au NP with an overall diameter of 8.9 nm [157]. This is attributed to the very low aspect ratio of the HGN [136,158]. When the shell thickness was kept constant and the overall diameter increased (6.2–12.2 nm) T_{osc} (5.5–16.0 ps) was found to increase linearly with increasing diameter [136]. The increase in the oscillation period associated with higher aspect ratio HGNs was attributed to the hollow cavity and a softening of the isotopic vibrations associated with the polycrystalline lattice of the shell [136,156].

3.2. The influence of laser mode and power

Another parameter involved in heat generation is the power of the operating laser as well as whether the laser is run in continuous wave (CW) or pulsed wave (PW) mode when interacting with nanoparticles [150,159–163]. While there is still some debate as to which mode is best, pulsed mode is generally considered more efficient than continuous mode for heating nanoparticles in photothermal applications [150,164–168]. It has been reported that additional time for electron–phonon relaxation is created between lapses in pulses, which leads to better heat generation [167]. This is attributed to competition between the cooling of the lattice and the rate of the nanoparticle absorption of light [169]. In contrast, the application of a CW laser is believed to dissipate absorbed energy into its environment as the temperature of the

nanoparticle increases due a relatively stable thermal relationship between the nanoparticles and solvent [99,164,165].

Prevo et al. investigated the effect of a femtosecond laser on hollow gold spheres of different sizes [170]. Previous work studying the effect of pulsed laser on nanoparticles showed that exposure to irradiation resulted in fragmentation of particles and the generation of new extinction peaks associated with the new population [161,169,171–173]. In this work, particles with diameters ranging from 20 to 50 nm with SPRs ranging from 550 to 750 nm were subjected to NIR pulsed light for 10 min at two different powers (350 and 700 μJ) [170]. For the higher power, regardless of size, all nanoparticles sintered and annealed in to solid spheres, producing a shift in their initial extinction peak to one that fell between 500–550 nm [170]. For the lower power, the hollow spheres broke in to asymmetric incomplete shells, oblate spheroids, rods and branched structures. These spheres also saw the loss of their initial absorption peak and the creation of a new peak at bluer wavelengths [170]. This determination of power dependence with respect to fragmentation is important when considering an application like drug delivery where it is necessary to induce the release of material from the inner cavity of the HGN through collapse of the external structure [174,175].

The effect of pulsed and CW mode laser on the spectral hole burning of HGNs has also been investigated [176]. Femtosecond pulsed laser at 810 nm and a repetition rate of 752 Hz was used to evaluate the impact on both the plasmonics and structural integrity of HGNs by varying the laser power using neutral density (ND) filters [176]. After exposure to three different powers, the NIR SPR associated with the sample before laser exposure decreased and additional peaks appeared [176]. Each power resulted in a distinct spectrum. In the case of the lowest power (ND 0.5) the initial peak at 810 nm was reduced slightly while a small peak at 672 nm grew. At the highest power (ND 0.1), the peak at 810 nm was reduced almost completely and two additional peaks were observed at 640 nm and 520 nm [176]. The growth of new peaks is attributed to the generation of both smaller HGNs and solid Au NPs created by HGN fragmentation. [177].

In contrast, when a CW mode laser was applied to the sample there was neither change in the intensity of the 810 nm absorption peak nor any additional peaks generated [176]. This indicates that the structural integrity of the HGNs was not altered as a result of laser exposure. Fig. 8 shows UV–vis data associated with HGNs following exposure to both pulsed and continuous mode lasers. It is clear to see that samples irradiated with pulsed light had their initial NIR absorbing peaks diminish as new blue-shifted peaks grew while HGNs irradiated with a continuous mode laser maintained their original NIR extinction peak [176].

The relationship between laser pump power, aspect ratio, the coupling constant g and hot electron relaxation lifetime has been investigated for HGNs [149]. Electron–phonon coupling efficiency can be described in part by the coupling constant g and is known to increase linearly with increasing S/V ratio [148,149,178–182].

Dowgiallo et al. found a linear relationship between increasing aspect ratio and the coupling constant g for HGNs [149]. It has been reported that low aspect ratio nanoparticles have g values comparable to their solid counterparts while high aspect ratio ones have enhanced g values [14,85,140,152,182]. In this work, as the aspect ratio increased from 3.5 to 9.5, the g value increased from $1.67 \times 10^{16} \pm 0.22$ to $3.33 \pm 0.45 \times 10^{16} \text{ W m}^{-3} \text{ k}^{-1}$, while solid NPs maintained an average g of $1.90 \pm 0.20 \times 10^{16} \text{ W m}^{-3} \text{ k}^{-1}$ over a range of diameters (20, 40, and 80 nm) [149]. As aspect ratio increased electronic relaxation time decreased, which was attributed to the large S/V area and enhanced electron–lattice interactions due to spatial confinement effects [36,149]. The relationship between aspect ratio, g and lifetime can be seen in Table 1.

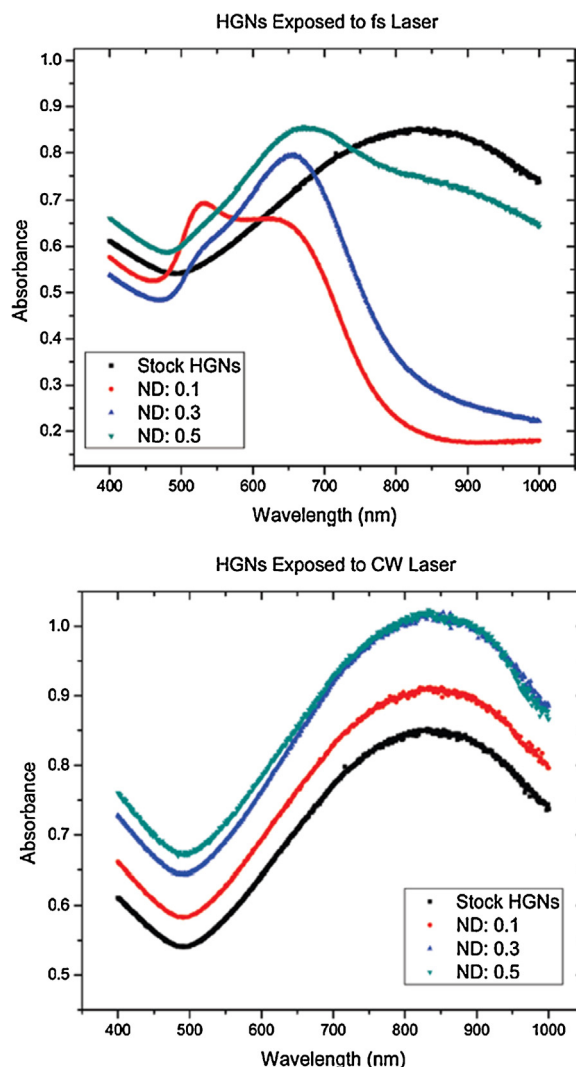


Fig. 8. UV–vis spectra of as-prepared and post hole-burning HGNs using different ND filters in the laser beam or different peak powers. HGNs exposed to the fs-pulsed mode laser (top) show the growth of new peaks after irradiation. HGNs exposed to CW mode laser maintain their original peak post-treatment with NIR light. (Reprinted with permission from reference [176]. Copyright 2010).

Table 1

Aspect ratio dependence of electron–phonon coupling and electronic relaxation lifetimes of various HGNs. (Reprinted with permission from reference [149]. Copyright 2011).

Sample	Aspect ratio	T_0 (ps)	G [$10^{16} \text{ W m}^{-3} \text{ K}^{-1}$]
A	3.5 (± 0.6)	1.12 (± 0.08)	1.76 (± 0.13)
B	5.1 (± 0.6)	1.18 (± 0.16)	1.67 (± 0.22)
C	5.4 (± 1.5)	0.97 (± 0.08)	2.03 (± 0.17)
D	6.5 (± 1.3)	0.90 (± 0.08)	2.19 (± 0.19)
E	6.7 (± 1.8)	0.91 (± 0.08)	2.16 (± 0.19)
F	7.2 (± 2.1)	0.80 (± 0.08)	2.45 (± 0.24)
G	7.8 (± 1.6)	0.69 (± 0.10)	2.82 (± 0.41)
H	8.3 (± 2.3)	0.65 (± 0.23)	3.01 (± 1.05)
I	9.0 (± 1.6)	0.65 (± 0.08)	3.04 (± 0.37)
J	9.5 (± 2.1)	0.59 (± 0.08)	3.33 (± 0.45)

Additionally, Dowgiallo et al. found that as laser pump power increased from 200 to 800 nJ per pulse, that hot electron relaxation times increased [149]. Fig. 9 shows bleach recovery kinetics for one HGN sample at seven different laser pulse intensities.

Harris et al. used variation in laser radiation to determine which size and aspect ratio for an HGN would produce the maximum surface heat flux and energy transfer between the particle

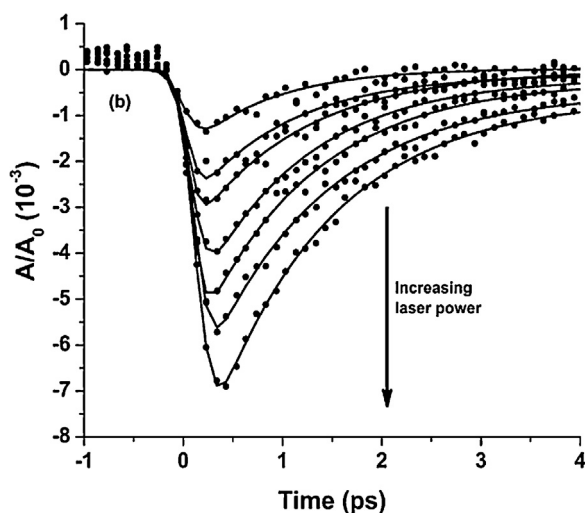


Fig. 9. Bleach recovery kinetics observed for seven laser pulse intensities (200 nJ to 800 nJ) at the minimum of the SPR band (630 nm) for an HGN with an outer diameter of 53.3 nm a shell thickness of 5.7 nm and an aspect ratio of 9.5. (Reprinted with permission from reference [149]. Copyright 2011).

lattice and its surroundings [183]. The computer program BHCOT was used to model absorption efficiency and heat flux [184]. In this work, two scenarios were investigated: irradiation by sunlight at 800 W/m² and irradiation by a monochromatic laser source of 50 kW/m² [183]. For laser illumination the optimum absorption efficiency of $Q_{\text{abs}} \sim 19$ occurred for an HGN having an outer radius of ~ 50 nm and an aspect ratio of 0.90. This corresponded to a maximum surface heat flux of 245 kW/m². In contrast a solid Au sphere with the same diameter had peak absorption efficiency almost a factor of 5 smaller ($Q_{\text{abs}} \sim 4$) and maximum surface heat flux of 50 kW/m². Under simulated sunlight the maximum surface heat flux of 175 W/m² occurred for an HGN with an outer diameter of 80 nm and an aspect ratio of 0.80, whereas a solid sphere with a diameter of 110 nm gave a surface heat flux of 150 W/m².

4. Photothermal therapies

4.1. Photothermal ablation (PTA) therapy

Photothermal ablation (PTA) is an attractive alternative to chemotherapy and invasive surgery for treating a variety of cancers and a number of excellent reviews have been published on the topic [5,53,119,167,185–190]. Briefly, noble metal nanoparticles, exhibiting NIR absorption in the appropriate size regime (20–100 nm) for biological applications, are modified with either an antibody or ligand specific to an antigen or receptor, on the surface of a tumor cell [38,53,190]. NIR absorbing particles are preferred since it is well known that blood and tissue are most readily penetrated by light in this wavelength region [191–193]. The bioconjugated nanoparticles are then introduced, either *in vitro* or *in vivo*, and allowed to incubate or circulate and bind to the tumor site.

Light on resonance with the absorption of the nanostructures is then used for excitation. Following excitation, electrons relax via electron–electron, electron–phonon, and phonon–phonon interactions [9,36,172,194]. During this process, most of the energy is converted to thermal energy [2,152]. Stronger light absorption leads to more heat generation.

Heat transfer from the nanoparticle to its surroundings, known as the photothermal effect, increases the local cell temperature which must reach a minimum of $\sim 40^\circ\text{C}$ for apoptosis to occur [189,195–197]. Hyperthermia arises from a number of mechanisms, including cavitation effects caused by microbubble

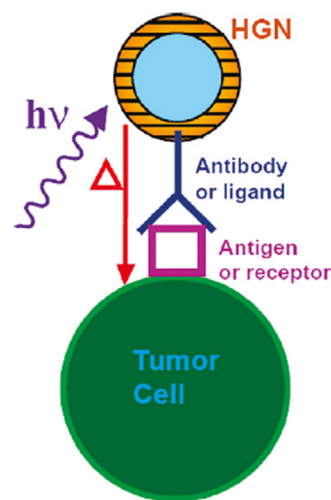


Fig. 10. A general overview of the PTA process. First a NIR absorbing HGN in the appropriate size regime is modified with either an antibody or ligand which is specific to an antigen or receptor on the surface of a tumor cell. Once the bioconjugated nanoparticles are bound to the cell, laser light on resonance with the HGN absorption wavelength are illuminated generating the conversion of kinetic energy into thermal energy which is then be transferred as heat to the surroundings via phonon-phonon interactions, leading to cell death. (Reprinted with permission from reference [53]. Copyright 2010).

formation, disruption of cell membranes and denaturation of proteins [198–200]. This process is a highly localized phenomenon and confined to only those regions specifically targeted by bioconjugated metal NPs [201–203].

Appropriate penetration of light through tissue must also be achieved in order to facilitate heat generation and cell death. Typically penetration in the range of 1–20 mm is sufficient for the ablation of cancer cells that are near the surface of the skin [160,191,193,204]. However, it has been reported that depths of 50–80 mm have been achieved [186,205]. Fig. 10 depicts the PTA process described above.

An early demonstration of photothermal therapy was reported by Halas et al. [160]. Using nanoshells with a 110 nm silica core diameter and a 10 nm Au shell, the authors reported significant reduction of human breast carcinoma epithelial cells (SK-Br-3) both *in vitro* and in a mouse model. Since then there have been many accounts of laser initiated hyperthermia using a variety of nanoparticles with solid Au spheres, cubes, stars, shells and rods all demonstrating successful results in photothermal applications [119,167,189,197,206–212].

However, as discussed previously, many of these structures suffer from inherent deficiencies if maximum efficiency is to be achieved. In general, solid structures have higher scattering efficiencies than hollow ones which means that there is less energy available to convert into heat in photothermal applications [15,29,158,213,214]. For example, it has been reported that silica-gold core-shell nanoparticles (150 nm diameter) had total extinctions that are comprised of only 15% absorption efficiency [215]. Shells also have broadened spectral line widths due to variation in size and shape within an ensemble and are considered cytotoxic due to the polymer core [190,216]. Rods, cubes, stars and aggregates, as noted earlier, will have reduced overlap with incident light because they have two or more resonances [18,35,48,55]. They are also synthesized with CTAB and other surfactants that are known to be cytotoxic [104,217,218]. Additionally, nanorods are known to be less effective at cell penetration and have significantly longer clearance times *in vivo* than spherical NPs [69,70,219,220].

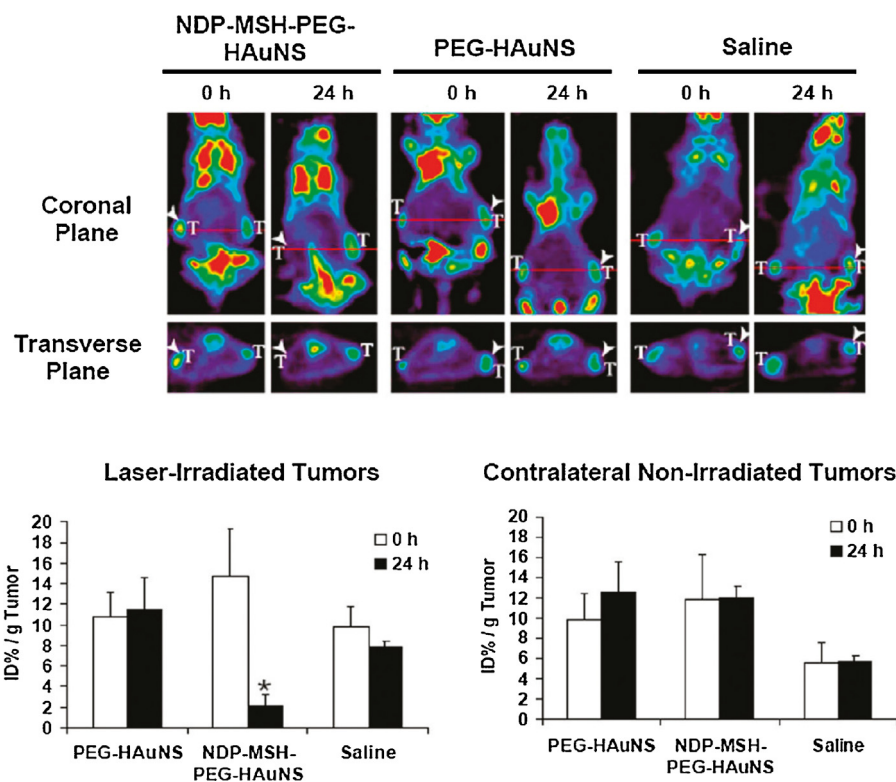


Fig. 11. *In vivo* photothermal ablation with targeted NDP-MSH-PEG-HGNS induced selective destruction of B16/F10 melanoma in nude mice. [^{18}F] Fluorodeoxyglucose positron emission tomography (PET) imaging shows significantly reduced metabolic activity in tumors after photothermal ablation in mice that were pretreated with NDP-MSH-PEG-HGNS, but not in mice pretreated with PEG-HGNS or saline. (^{18}F)-fluorodeoxyglucose PET was conducted before (0 h) and 24 h after near-IR laser irradiation (0.5 W/cm² at 808 nm for 1 min), which was commenced 4 h after i.v. injection of HGNS or saline (T for tumor). Arrowheads in the figure indicate tumors irradiated with near-IR light. (^{18}F)-fluorodeoxyglucose uptakes (%ID/g) before and after laser treatment are shown graphically at the bottom. (Reprinted with permission from reference [72]. Copyright 2009).

4.2. PTA with HGNS

There has been an increasing interest in using HGNS in PTA applications [72,78]. In addition to their small size, spherical shape, biocompatibility, and lack of susceptibility to photobleaching, their extinction peaks can be easily tuned to the NIR [60,78,79,221]. Additionally, the enhanced near field energy associated with their surface plasmon resonance and thin shells, which produce high absorption cross-sections, makes them ideal nanostructures for PTA.

The Zhang Lab is currently investigating how size affects both the performance of HGNS as a photothermal coupling agent and the performance of HGNS in nanoparticle-mediated PTA of oral squamous cell carcinoma. Lindley's experiments are being performed using HGNS of different diameters with constant SPR (~800 nm to be compatible with the NIR window). Control of the cobalt scaffold size and gold shell deposition is also being investigated (Lindley, unpublished).

The first demonstration of HGN viability in PTA was reported in 2008 by Melancon et al. [78]. In this work, the authors have attached monoclonal antibody epidermal growth factor receptor (EGFR) to 30 nm HAuNS in order to target the A431 oral cancer cell line both *in vitro* and *in vivo*. Selective uptake of the bioconjugated NPs by the tumor cells was demonstrated by imaging scattered light from the HAuNS. Ablation experiments were performed using a diode laser centered at 808 nm with 40 W/cm² of power for 5 min [78]. Cells treated with anti-EGFR-HAuNS plus laser selectively destroyed tumor cells, while those exposed to anti-EGFR-HAuNS alone, laser alone, or IgG-HAuNS plus laser did not. Heat generation was also evaluated and after 4 min of irradiation cells were shown to have temperature changes ranging from 9.8 to 16.5 °C [78].

In 2009, Lu et al. reported the successful HGN mediated ablation of melanoma *in vivo* using a mouse model [72]. Here, NIR absorbing HGNS with an average outer diameter of ~43.5 nm and a shell thickness of 3–4 nm were stabilized with polyethylene glycol (PEG) and attached to an α -melanocyte-stimulating hormone (MSH) analog, [Nle⁴,D-Phe⁷]a-MSH (NDP-MSH), targeting the melanocortin type-1 receptor over-expressed in melanoma. PEG has shown to be the most effective capping agent for HGNS, stabilizing the nanoparticles against aggregation, caused by both increased salt concentration (up to 5 M) and changes in pH [222,223]. The intracellular uptake of bioconjugated HGNS was confirmed by both excised tissue and by (^{18}F)-fluorodeoxyglucose positron emission tomography [72]. The mechanism of cellular uptake was later determined to be, by the same author, initiated by agonist receptor binding followed by transcellular transport by tumor vessels, of the NDP-MSH-conjugated PEGylated HAuNS (NDP-MSH-PEG-HAuNS).

NIR laser ablation was performed using an 808 nm laser with output energy of 32 W/cm² for 3 min [72]. Cancer bearing mice treated with (NDP-MSH-PEG-HAuNS) plus laser saw a 66% necrotization of their tumors compared to mice treated with either PEG-HAuNS plus laser or saline which showed negligible cell death [72]. Fig. 11 shows (^{18}F)-fluorodeoxyglucose positron emission tomography (PET) of nude tumor bearing mice pre and post-laser treatment with conjugated HGNS used in this study.

4.3. Multi-modal treatments

While PTA has proven to be an effective method of eradicating cancer cells both *in vitro* and *in vivo*, its application remains limited by the fact that the diffusion of heat through tissue at increasing depths of penetration is not uniform [198,208,224]. This means that

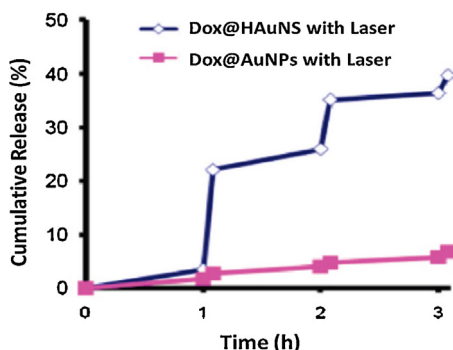


Fig. 12. Release of DOX from DOX@HAuNS and DOX@AuNPs following exposure to NIR laser. (Reprinted with permission from reference [224]. Copyright 2010).

some portions of the tumor cells will reach an appropriate temperature to induce apoptosis and some will not. This is particularly true for tumors peripheral to large blood vessels which facilitate rapid dissipation of heat through the circulation of blood [206,225,226]. In order to improve efficiency, many researchers have combined PTA with drug delivery to enhance the destruction of cancer cells during treatment.

Traditionally drugs in photothermal therapies are delivered via polymeric structures or liposomes [99,227–232]. However, these delivery agents are hindered by several factors. Polymers are cytotoxic and degrade *in vivo*, promoting immunogenic reactions, and liposomes are prone to leakage which results in decreased efficiency of biomolecule delivery [231,233–237].

HGNs are playing a larger role in multi-modal therapies due to the combination of their unique optical properties, appropriate size regime, ease of bioconjugation and increased success rate of crossing tumor vessel walls [70,72,74]. Their hollow cavities are convenient for loading and delivering drugs and biomolecules *in vivo*. Since they are comprised of gold, they are also stable against photobleaching and their thin shells lead to enhanced absorption efficiencies.

4.3.1. Cancer drug delivery plus PTA

In 2010, You et al. reported that the use of hollow gold nanostructures showed a 3.5–4.0 fold increase in the payload of doxorubicin (DOX) when compared to solid Au nanoparticles of the same size [224]. In this work, MDA-MB-231 breast cancer cells were targeted by polyethylene glycol (PEG) stabilized 40 nm NIR absorbing HGNs loaded with $\sim 1.7 \mu\text{g DOX}/\mu\text{g Au}$ ($\sim 63\%$ by weight). Tumor bound HGNs were then subjected to NIR laser illumination with a power output of $4.0 \text{ W}/\text{cm}^2$ for 5 min, 1-h post-injection [224]. Cell cultures were used to quantify the *in vitro* release of the drug post-laser and maximal DOX release (16.7%) was observed for pH 5.0. It can be seen in Fig. 12 that the cumulative release of DOX@HAuNS was significantly higher than for that of DOX@AuNPs following exposure to NIR laser [224].

In a related study, the pharmacokinetics and biodistribution of DOX loaded NP3 conjugated NIR absorbing HAuNS targeting both human MDA-MB-231 breast cancer and A2780 ovarian cancer were evaluated *in vitro* and *in vivo* using dual isotope radio labeling [80]. Following incubation, the bioconjugated and cell bound HGNs were exposed to NIR laser with $32 \text{ W}/\text{cm}^2$ power output for 5 min. Release of DOX was monitored by ^{64}Cu radiolabeling. In evaluating post-treatment for cytotoxicity, mice treated with free DOX suffered the greatest toxicity, with 3/5 subjects dying during the course of treatment from vacuolar cardiomyopathy. In contrast, mice that were treated with DOX delivered via HAuNS had similar histopathologic features in their hearts as those treated with saline [80].

In an extension of this work, DOX@HAuNS were used to target EphB4, a member of the Eph family of receptor tyrosine kinases [238]. EphB4 is over-expressed in the cell membranes and angiogenic blood vessels of multiple cancers including prostate, colon and bladder. The majority of mice (6/8) treated with targeting DOX@HAuNS (T-DOX@HAuNS) plus NIR laser treatment showed cancer which regressed completely 22 days post treatment [238]. Tumor temperatures were measured 5 min post-laser irradiation at $3 \text{ W}/\text{cm}^2$ for 5 min and found to be $\sim 53^\circ\text{C}$. In contrast, mice treated with nontargeted DOX@HAuNS plus laser, HAuNS plus laser or saline all showed viable tumor activity several weeks after treatment.

In 2012, Gupta et al. used biodegradable microspheres (MS) containing hollow gold spheres (HAuS) and paclitaxel (PTX) [MS-HAuNS-PTX] to determine if drug delivery by targeting HGNs carrying PTX could be used in conjunction with NIR laser irradiation (MS-HAuNS-PTX-plus-NIR) to enhance the efficiency of cell death in a rabbit model with hepatic cancer [239]. These results were compared to those of rabbits treated with bioconjugated HGNs without PTX plus laser (MS-HAuNS-plus-NIR). The authors observed significantly greater tumor necrosis for animals receiving MS-HAuNS-PTX-plus-NIR ($44.9\% \pm 15.4\%$) than for MS-HAuNS-plus-NIR ($13.8\% \pm 6.9\%$).

Laser experiments were performed using 1.5 W of power for 1, 3, and 5 min [239]. At each interval of time, temperature changes were observed at the border of the lesion and at the tip of the laser fiber [239]. The laser fiber showed changes in temperature of 8.6°C at 1 min, 12.4°C at 3 min, and 13.9°C at 5 min. Temperature changes around the lesion were reported as 2.3°C , 8.5°C , and 2.6°C at the 1, 3, and 5 min time points.

4.3.2. Photothermal transfection

Photothermal transfection, or down-regulation, is a widely used method of delivering molecules which interfere with the expression of undesired genes that cause replication of disease particularly in cells where there is tumor formation [240–244]. The technique employs a NIR light trigger to facilitate site specific silencing through biomolecule delivery and the conversion of electronic energy to heat [245–247]. Nanocarriers typically target proteins, peptides, nucleic acids, DNA, and RNA [71,241,248–253]. Polymeric structures and liposomes are usually employed as carriers, however, as stated above; polymers are large and cytotoxic and liposomes prone to leakage [254–256].

As a result, researchers have been investigating alternatives and HGNs are beginning to gain some attention in the field [79,177,257]. For example, Braun et al utilized a 40 nm diameter hollow gold nanosphere with a 3 nm shell to temporally and spatially control cellular delivery of RNAi for gene silencing through a direct endosome release mechanism activated by pulsed laser [79]. RNAi desorption from the HGN, which is known to be initiated by cleavage of the Au-S bond, was monitored through Cyanine 3 (Cy3) fluorescence, which is partially quenched when attached to HGNs and unquenched when not associated [79,258,259]. In another study, Wu et al used HGNs as “nanosonicators” to trigger the release of a dye from inside liposomes in a proof of concept study demonstrating near instantaneous release of liposome contents with precise spatial and temporal control *in vitro* [257].

NIR light induced NF- κ B down-regulation through folate receptor targeting HGNs carrying small interfering RNA (siRNA) recognizing the NF- κ Bp65 subunit over-expressed in HeLa cervical cancer has been demonstrated both *in vitro* and *in vivo* [177]. The use of micro-positron emission tomography and electron microscopy were used to confirm significant uptake of bioconjugated HGNs by endocytic vesicles (endosomes and lysosomes) within the tumor [177]. Successful down regulation was attributed to the simultaneous structural deformation of the HGN under NIR light,

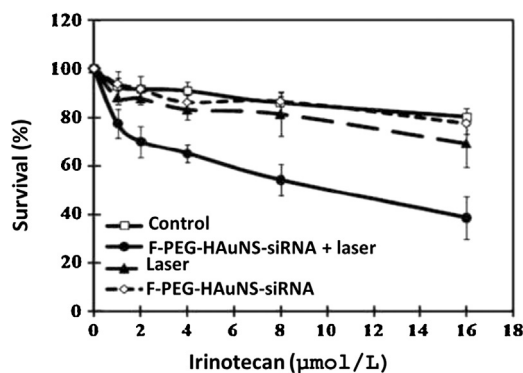


Fig. 13. Percent cell survival of control, F-PEG-HAuNS-siRNA + laser, laser alone and F-PEG-HAuNS-siRNA alone. (Reprinted with permission from reference [177]. Copyright 2010).

which was confirmed by UV–vis spectral changes in SPR, and the breakage of the Au–S bond, due to heat, which resulted in the release of siRNA to the cytosol [177]. This mechanism has been described previously in photothermal transfection experiments involving DNA and is attributed to hot electron thermalization of the nanoparticle lattice [243,260,261]. Fig. 13 shows the percent tumor cell survival for several conditions and a control used in the experiments. It can be seen that cells treated with F-PEG-HAuNS-siRNA + laser had significantly enhanced cell death and that siRNA mediated p65 gene silencing significantly enhanced chemosensitivity of HeLa cells to irinotecan [177].

Lu et al. also used polyacrylamide gel electrophoresis (PAGE) to evaluate the release of siRNA in to the cytosol for two conditions: cell bound bioconjugated HGNS that had either been treated with NIR light or not [177]. Only negligible amounts of siRNA were released for HGNS that did not receive laser treatment. However, near complete release of siRNA was observed when HGNS were exposed to NIR light [177]. The release of siRNA from HGNS was correlated to significant inhibition of the cellular expression of p65. The distribution and elimination half-lives for thiolated poly (ethylene glycol) HAuNS and PEGylated HAuNS were 1.38, 71.82 h, respectively.

5. Surface enhanced Raman scattering (SERS) and electromagnetic (EM) field enhancement

Since its discovery in the late seventies SERS, which relies on a roughened noble metal substrate to enhance the sensitivity of Raman detection, has become a powerful tool in the early identification and diagnosis of disease [262–272]. The highly localized EM field of the metal, due to SPR, is known to enhance the Raman signal by 5–10 orders of magnitude [273–276]. Aggregation of metal nanoparticles can also be employed to produce significant SERS enhancement through the generation of hot spots which result from EM coupling between particles in near field proximity to one another [56,64,182,198,277,278].

The most common substrate used in SERS applications is Ag [212,273,279–281]. However, Ag is considered unstable, degrades *in vivo* and is typically synthesized with cetrimonium bromide (CTAB), which is considered cytotoxic [282–284]. Additionally, it has been demonstrated that the peak intensity ratios of the Raman signal change significantly when silver aggregates are used leading to inconsistent results and poor reproducibility [276,285–287].

It has been reported that HGNS show improved SERS activity when compared to Ag aggregates [287,290,291]. When Schwartzberg et al. compared HGNS to silver aggregates, the Rayleigh scattering intensity of HGNS showed nearly a 10-fold improvement over Ag [290]. Fig. 14 shows the SERS intensity

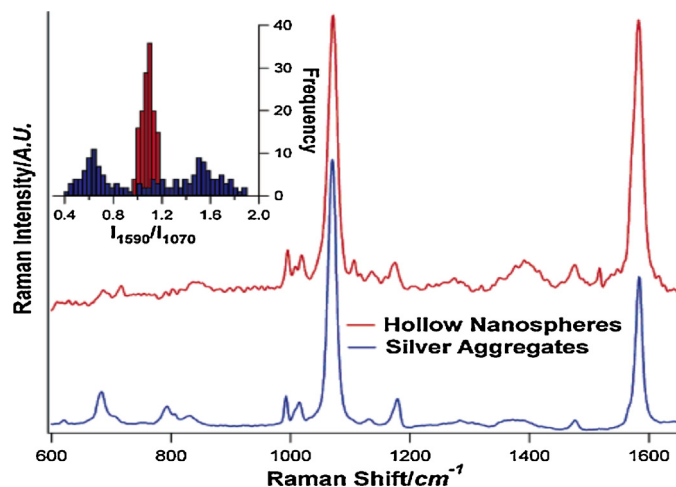


Fig. 14. Single particle SERS spectrum comparing HGNS (red top trace) and Ag aggregates (blue bottom trace). The inset is a histogram of the relative intensity of the two most prominent peaks of the Raman reporter molecule 4-mercaptobenzoic acid (MBA) at 1070 and 1590 cm^{-1} of 150 HGNS (red bars) and 150 silver aggregates (blue bars). (Reprinted with permission from reference [290]. Copyright 2006).

spectra for both HGNS and Ag aggregates bound to the Raman reporter molecule 4-mercaptobenzoic acid (MBA). There is significant signal enhancement for the HGNS. Furthermore, all the peak intensity ratios for the HGNS fall within 0.9 and 1.1 [290]. This represents a statistical distribution of 5%. In contrast, the Ag NPs exhibit a 45% statistical distribution (0.5–1.7) with respect to consistency. This inconsistency is due to the randomness of aggregation which, depending on size and shape, will produce variation in the EM field associated with the ensemble [64,65,288–290].

Lee et al. also found that antibody conjugated HGNS targeting the HER2 breast cancer marker over-expressed in MCF7 cells had much better homogeneous scattering properties with more consistent intensity ratios than bioconjugated Ag aggregates targeting the same cells [287]. For HGNS the intensity ratios ranged from 0.8 to 1.4 compared to 0.9 to 3.1 for Ag. Both Schwartzberg and Lee attribute the enhancement of the Raman signal and consistency of intensity ratios to the uniform structure and narrow plasmon dispersity of HGNS [287,290].

5.1. Plasmon coupling in aggregates for SERS

In order to optimize HGN use in SERS based applications it is critical to understand the effect of their structure, size, and aggregation on EM field enhancement. In general, aggregation intensifies the second harmonic generation of HGNS in contact with one another, effectively combining their collective energy to generate new photons with twice the frequency and half the wavelength [292–295]. HGN aggregates are also known to exhibit both hybridized plasmon modes, which are the result of surface plasmon interactions with cavity plasmon modes, and collective charge transfer resonances [296–298]. However, even when not in direct contact with one another there is an intensification of the dipole charge at the interparticle gap of nanoparticle aggregates in near field proximity [8,299–301]. For example, Xu et al. observed that the junction between two nanoparticles 1 nm apart exhibited an EM field enhancement of 10^{10} compared to an individual particle [302]. The charge transfer between two HGNS in a dimer interacting with an EM field polarized parallel to the interparticle axis is shown in Fig. 15. It can be seen that the two surfaces in contact with each other are polarized with opposite signs which contributes to the enhancement of charge-transfer between particles [303].

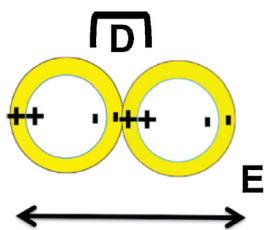


Fig. 15. Schematic representation of stable charge-transfer plasmon configuration between a contact dimer. The incident EM field is polarized parallel to interparticle axis of the two HGNs. The combined interfacial shell thickness is given by D . (Reprinted with permission from reference [303]. Copyright 2010).

It has been reported that the majority of HGN aggregates are made up of surface necking dimers, which exhibit a longitudinal resonance and an EM field localized along the outer surface of the NPs with smaller contributions from the cavity surface [304]. This energetic distribution is thought to be the result of complex intercavity interactions including the formation of charge transfer plasmon modes [303]. In contrast, HGN dimers having surface-surface contacts exhibit their highest energy in the conical region of the particle junction [304]. Fig. 16 shows electric field simulations for the interaction of various particle dimers within an

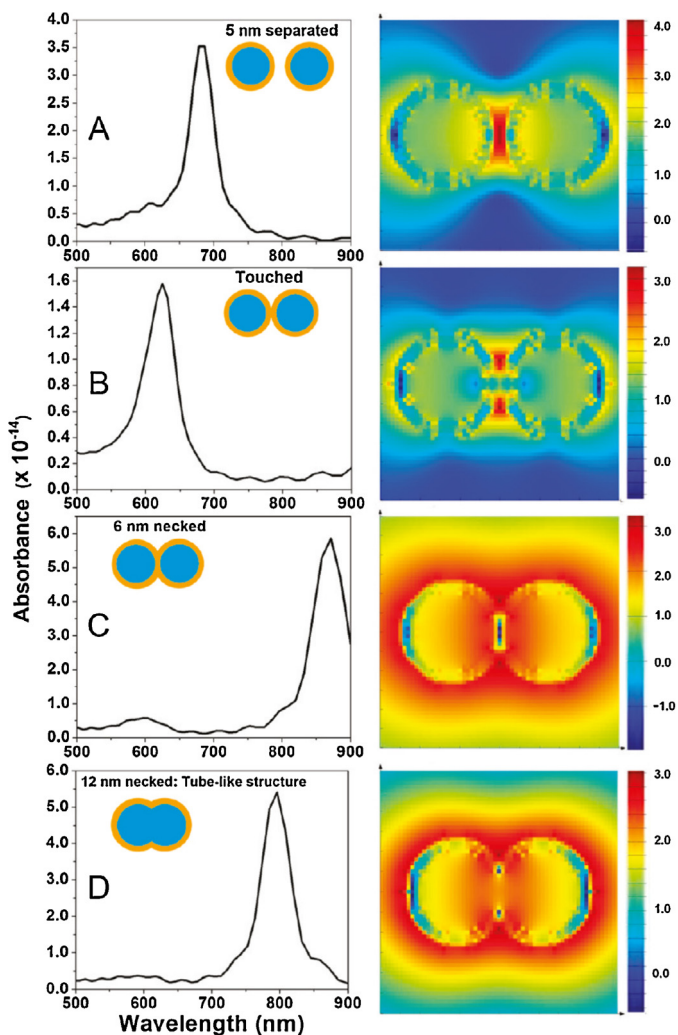


Fig. 16. Simulated analysis of SPR frequency and EM field generation for: (A) spatially separated HGNs, (B) point contact dimers, (C) surface-necked dimers, and (D) peanut-shaped coupling. (Reprinted with permission from reference [304]. Copyright 2015).

aggregated HGN system that were observed by both 2D and 3D electron microscopy [304]. These simulations represent modes of individual dimeric structures and not the aggregate as a whole. The corresponding impact of differences in dimerization on SPR is also shown using UV–vis extinction spectra.

The SPR of HGNs can be red or blue-shifted depending on dimer interactions within aggregates [44,134,304,305]. Dimers that were separated by 1.2 nm have their EM energy polarized at the interparticle axis and between the gap with a red-shifted SPR (55 nm) compared to similarly sized (30 nm core/4 nm shell) isolated HGNs [304]. Both surface necked and peanut shaped dimers also exhibited red-shifted extinction peaks with EM energy concentrated on the outer surfaces. In contrast, point contact (surface–surface) dimers experienced blue-shifted absorption spectra.

Chandra et al. used thiol mediated aggregation to study the experimental impact of aspect ratio (3.5–11.7) on the plasmonic response of HGNs [303]. Aggregation initiated with ethanedithiol produced contact dimers with substantially blue-shifted SPR, while those treated with cysteine produced large extended structures of spatially separated dimers having interparticle gaps ≥ 1 nm and red-shifted SPR. While the authors found no direct correlation between aspect ratio and plasmonic response, they observed a trend correlating shell thickness and SPR shift.

As shell thickness decreased for contact dimers generated by ethanedithiol, the change in absorption shifted to shorter wavelengths [303]. This blue-shift is believed to be the result of delocalized electrons confined within the cluster and the interactions of antibonding or higher energy HGN modes [307]. However, for contact dimers with shells ≥ 7 nm, no significant spectral shift was reported [303]. In comparison all cysteine induced aggregates with interparticle gaps ≥ 1 nm showed red-shifted absorption regardless of shell thickness. The red-shifted SPR is attributed to the generation of symmetric coupling of the bonding modes between the surface SPR and the inner cavity plasmon modes which lowers the energy of the symmetric modes of the dimer [301,308].

Xie et al. reported that HGNs with thicker shells, which have enhanced scattering cross-sections, generated greater SERS intensity whether they were on resonance or aggregated [44]. This is because thicker shelled HGNs are known to bear the majority of their EM field concentration at the conical region of the particle interface while thinner shelled HGNs have significant energy centered at their cavity walls [303].

5.2. First hyperpolarizabilities (β)

Raman scattering results from the induced dipole oscillations in a material as it interacts with an applied EM field. The greater the propensity of a molecule to generate a dipole, the more intense the plasmonic oscillations will be and the larger the signal enhancement [270]. For this reason, evaluating the first hyperpolarizability (β) of a nanostructure is useful since β , which is a measure of how easily a dipole is induced in a molecule in the presence of an electric field, is correlated with Raman signal intensity [309].

When HGNs of different sizes were compared to solid Au using two-photon Rayleigh scattering (TPRS) to measure their 1st hyperpolarizabilities (β), it was found that the β values of the HGNs greatly exceeded those of the solid NPs [134,306]. HGNs with overall diameters of ~ 30 and ~ 78 nm and shells ~ 8 and ~ 11 nm had β values of 5.4×10^5 ($\times 10^{-30}$ esu), 63×10^5 ($\times 10^{-30}$ esu) while 20 nm solid Au NPs showed a β value of 2.4×10^5 ($\times 10^{-30}$ esu) [306]. This is not surprising since β is known to scale linearly with surface area [309]. For comparison, the first hyperpolarizability of an HGN with ~ 80 nm diameter is 3 times that of a solid Au nanoparticle of the same size and ~ 1.5 times that of a solid Au nanoparticle with a 30 nm diameter [86,310].

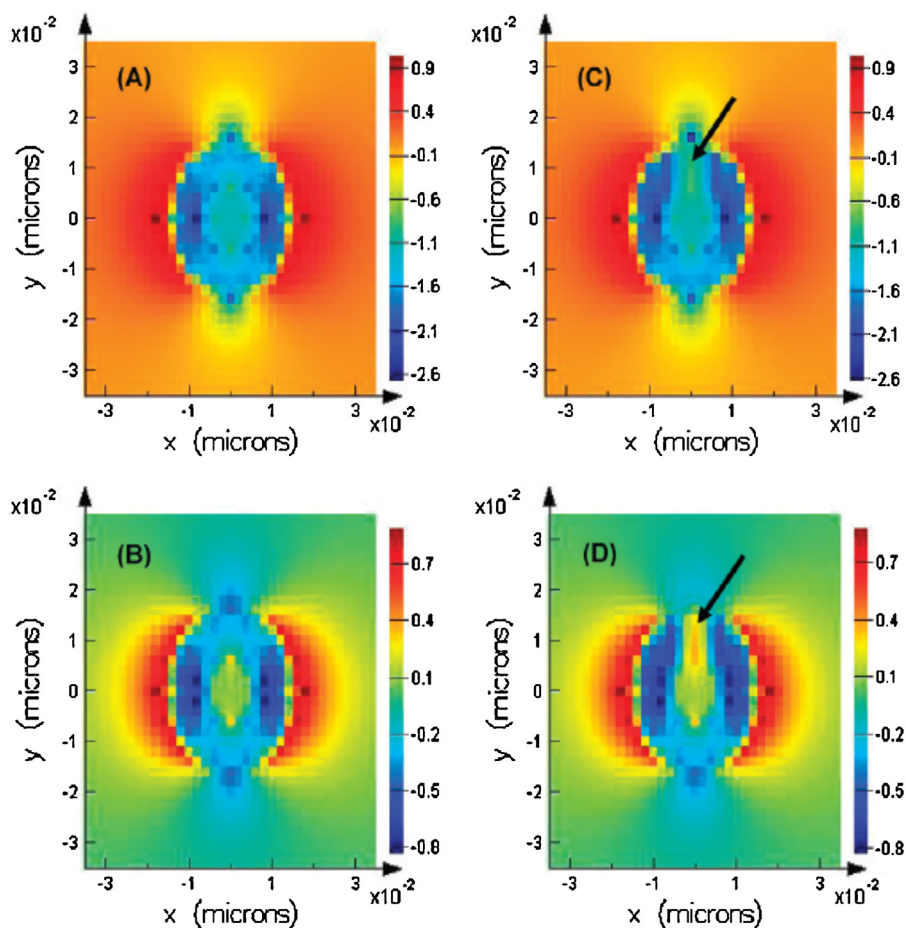


Fig. 17. Spatial EM field maps for HGN without (A and B) and with (C and D) a single pinhole (3 nm radius) defect at fundamental (A and C) and second-harmonic (B and D) wavelengths. The key correlating color to electric field intensity (in logarithmic scale) is shown to the right of each respective plot. The arrows point to the pinhole location. EM field enhancement at the pinhole region can be seen at the second harmonic wavelength (D). (Reprinted with permission from reference [306] Copyright 2010).

Another factor contributing to larger HGN β values is the presence of pinholes, which are known to generate hot spots, particularly when the pinhole axis is perpendicular (or near perpendicular) to the applied polarized light [290,311]. Fig. 17 shows the finite difference time domain (FDTD) simulated EM fields generated by an HGN with and without a single 3 nm pinhole [306]. It can be seen that the electric field is amplified around the pinhole. This enhancement was not observed for 30 nm solid gold nanoparticles used as a control in the experiment. The concentration and intensification of the oscillating EM field found in HGNS is attributed to an increase in surface to volume and charge to volume ratios found at both the inner and outer cavity dielectric surfaces [82,304,306].

5.3. SERS immunoassays

SERS based immunoassays utilizing noble metal substrates are rapidly becoming the preferred choice for detection of biological markers [73,119,128,160,312–314]. They are considered to have many advantages over traditional enzyme linked immunosorbent assays (ELISAs) which are considered tedious, time consuming, and rely on the use of toxic and unstable fluorescent dyes and quantum dots (QDs) [282,315–317]. It is known that SERS has equal or in some cases a greater enhancement of Raman signal when compared to fluorescent markers and that SERS metal substrates produce spectral line widths which are 10–100 times narrower compared to fluorescence [64,318,319]. This means the technique can be used where high selectivity and multiplexing (targeting two analytes at

once) is called for since the resolution between peaks will be well defined [320–332]. In addition, the short Raman scattering lifetime prevents photobleaching and quenching [312,323,324].

Solution based immunoassays overcome the slow diffusion kinetics and poor limit of detection (LOD) associated with conventional assays [73,319,320]. For example, the lung cancer carcinoembryonic antigen (CEA) was targeted using HGNS as a probe [325]. Magnetic beads were employed as a solution based support substrate to form a sandwich immunocomplex. The authors enhanced the sensitivity of detection of CEA by a factor of 100–1000 compared to a conventional enzyme-linked immunoassay [325]. The high sensitivity is attributed to the intensification of the EM field by pinhole generation of hot spots and the large scattering cross-section of the HGNS [82,290].

In an extension of this work, Chon et al. reported the simultaneous detection of CEA and α -fetoprotein (AFP), both over-expressed in many cancers, with one excitation wavelength of light [326]. Again, HGNS were used as a probe along with monoclonal antibody-conjugated magnetic as the solution based substrate to generate a sandwich type immunocomplex between the HGNS, CEA, and AFP. Fig. 18 shows the SERS spectra associated with the detection of both cancer markers at varying molar ratios. This multiplexing assay showed great sensitivity in detecting both markers in blood serum with the LOD for CEA being 5 ng/ml and that of AFP being 20 ng/ml [326]. The enhanced LOD is due to the presence of surface pinholes generating hot spots and plasmon coupling between both the inner and outer cavity and EM coupling between neighboring particles in the near field [297,298,302].

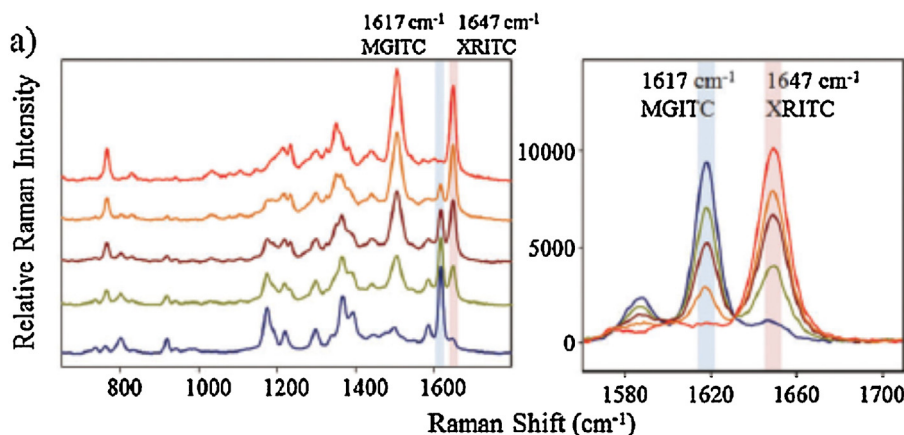


Fig. 18. SERS spectra of duplex cancer marker mixtures at different molar ratios. The molar ratios of CEA to AFP are 1:0, 3:1, 1:1, 1:3, and 0:1 from top to bottom. (Reprinted with permission from reference [326]. Copyright 2011).

5.4. SERS nanotags

A novel tracer, glucose oxidase (GOD)-functionalized HGNs encapsulating GOD ($\text{Au}_{\text{shell}}\text{@GOD}$) has been reported by Song et al. [298]. This tracer was designed to label the ferrocenemonocarboxylic-grafted secondary antibodies ($\text{Ab}_2\text{@Fc}$) of tumor markers using carboxyl group functionalized multi-wall carbon nanotubes (MWCN) as a platform. The electrocatalytic activity of the GOD- $\text{Au}_{\text{shell}}\text{@GOD}-\text{Ab}_2\text{@Fc}$ bioconjugated was tested against three sets of bio-recognition using chronoamperometry and was found to show the greatest current shift [298]. The ferrocene mediated electron transfer between GOD and the electrode surface along with high concentrations of GOD particles associated with the surface and cavity of the HGNs lead to enhanced signal amplification and enhanced detection along with the increased charge transport ability of the multi-walled carbon nanotubes (MWCN) [298].

It is known that depth of tissue penetration increases at longer wavelengths due to increased scattering and reaches a maximum at $\sim 1300\text{ nm}$ [327–331]. For this reason, it is necessary to develop red-shifted tags capable of reaching deep tissue in order to optimize diagnosis and treatment of disease. When Kobat et al. compared two excitation wavelengths (775 and 1280 nm) using two photon fluorescence microscopy (TPM) to label and image mouse blood vessels *in vivo* and *ex vivo*, the authors found that high contrast images obtained by using 1280 nm excitation had the twice the depth penetration as those obtained at 775 nm [332]. Recently, Bedics et al. developed an extreme red-shifted SERS nanotag comprised of chalcogenopyrylium dyes containing phenyl 2-thienyl and 2-selenophenyl substituents (with absorption wavelengths of 1064 nm) on the surface of HGNs (SPR = 720 nm) for use with 1280 nm laser excitation [333]. The limit of detection was found to be in the picomolar range for all 14 dyes used in the study and sensitivity of detection was attributed in part to the enhanced EM field associated with the HGNs.

6. Imaging

Non-invasive biological imaging has been used for decades to accurately visualize structures *in vivo* and to diagnose and help treat disease [67,96,334–339]. Common techniques include near infrared fluorescence (NIRF), positron emission tomography (PET), optical acoustic tomography (OAT), photo acoustic tomography (PAT), and magnetic resonance imaging (MRI) [338,340–343]. Typically QDs, fluorescent dyes and iodinated agents are used

as contrast agents and some methods call for the use of radioactive isotopes [343–349]. Unfortunately, each of these agents has its own drawbacks when used in biological applications.

As discussed above, QDs and dyes have issues related to biological incompatibility and lack of stability to photodegradation [342,350,351]. Additionally, QDs have been shown to remain in major organs for months after injection producing immunogenic reactions *in vivo* [352–355]. Iodinated agents are also less than ideal because of their biological toxicity and short circulation time *in vivo* [356–358]. For example, Kim et al. reported that when Ultravist, an iodine based contrast agent, was used in a rat model the circulation time was less than 10 min compared to that of 30 nm spherical Au nanoparticles which circulated *in vivo* for over 4 h [356].

Gold nanostructures are often used to overcome the limitations found with standard contrast agents [359–362]. In addition to their biocompatibility, Au nanoparticles have longer *in vivo* circulation times during the imaging process and in some cases faster elimination time post-procedure [356,363–365]. Additionally, since the atomic number of Au is higher than that of iodine, Au nanostructures have higher absorption efficiencies which means that *in vivo* contrast will be enhanced [35,356,364,366].

HGNs are a natural extension of Au nanoparticles used in imaging. As noble metal structures, they have enhanced EM field strength because of their plasmon resonance, and surfaces can be easily functionalized to target biomolecules. They are also resistant to photobleaching and have molar extinction coefficients (ϵ) that are larger than those of dyes and QDs [35,38,177,367]. For instance, Lu et al. recently reported that a 40 nm HGN with a 2–3 nm shell and an SPR of 800 nm has a molar absorption coefficient of $1.4 \times 10^{11} \text{ M}^{-1} \text{ cm}^{-1}$ [177]. In comparison, fluorophores have ϵ in the range of 5.0×10^3 to $2.0 \times 10^5 \text{ M}^{-1} \text{ cm}^{-1}$ and QDs have molar absorption coefficients $\sim 1 \times 10^5 \text{ M}^{-1} \text{ cm}^{-1}$ making both far less effective as contrasting agents [261,368,369].

Photoacoustic imaging is a hybridized technique combining non-ionizing radiation and ultrasonic detection [292,370–372]. The photoacoustic signal is considered inherently weak due to the low intrinsic absorption of oxyhemoglobin and deoxyhemoglobin in the NIR [177,373–375]. However, high spatial resolution and enhanced sensitivity were found to accompany the use of HAuNS in the PAT experiment reported by Lu et al. [177]. In this work, the authors conjugated thiolated PEG to the surface of NIR absorbing HAuNS and used them to image living mouse brain vascular [177]. One half of the mice subjects were injected with

PEG-HAuNs and the other half with saline. The researchers were able to visualize brain blood vessels as small as $\sim 100 \mu\text{m}$ for up to 2-h post-injection in the mice that had been treated with PEG-HAuNs at concentrations as low as $\sim 20 \text{ pM}$ [177]. Furthermore when the researchers compared the photoacoustic brightness of HGNs to other common imaging agents, it can be seen in Fig. 19 that the use of HGNs produced significant optical enhancement.

In another recent report, HGNs were used as a contrast agent to identify the primo vascular system (PVS) in a rat model [376]. Previously, visualization of the PVS, particularly the IL subtype (one of six in the PVS) has been challenging due to the small pore size ($20\text{--}50 \mu\text{m}$). In this work, the authors compared two types of HGNs: $50\text{--}70 \text{ nm}$ (SPR 675 nm) and $111\text{--}125 \text{ nm}$ (SPR 800 nm) to Alcian blue dye [376]. The HGNs appeared either turquoise or green in order to provide good contrast to the red of hemoglobin. Rats injected with both types of HGNs showed a 95% success rate in the visualization of the PVS within 10 min [376]. In contrast, rats injected with Alcian blue dye showed only a 20% visualization success rate and the time period for visualization, when successful, was much longer. As a result of being able to visualize the system, researchers were able to harvest stem cells from the IL-PV using acupuncture needles in 18/19 rat models. Fig. 20 shows images of the PVS visualized after HGNs were used as contrast agents.

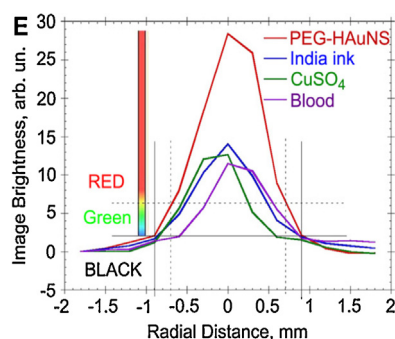


Fig. 19. Quantitative analysis of photoacoustic image brightness through cross section of blood (O.D. 1.6), CuSO_4 (O.D. 2.0), India ink (O.D. 0.8) and PEG-HAuNS (O.D. 0.7). (Reprinted with permission from reference [177]. Copyright 2010).

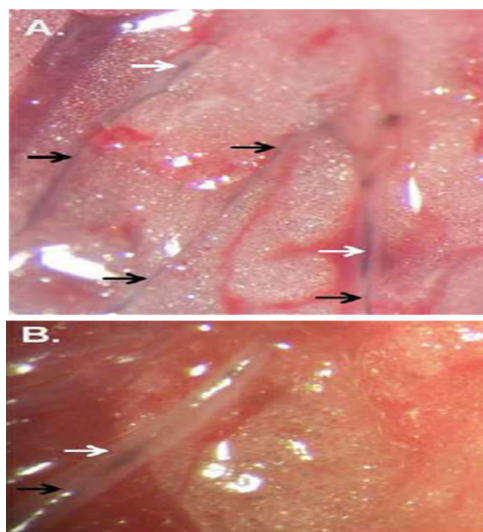


Fig. 20. (A) Image of multiple LVs with IL-PVS (black arrows) and PNs (white arrows) in rat contrasted with HGNs. (B) High magnification image ($40\times$) of IL-PV (black arrow) with PN (white arrow) contrasted by HGNs. (Reprinted with permission from reference [376] Copyright 2015).

7. Concluding remarks

Over the last decade, significant advancements have been made in understanding how the plasmonic response of HGNs can be tuned through synthesis to produce particles that are useful for a wide variety of applications including bio-diagnostics, bio-delivery and photothermal therapies. The study of plasmon coupling, collective charge transfer, and the EM enhancement associated with aggregation, pinhole generation, surface morphology, size, and aspect ratio have demonstrated that HGNs exhibit a number of interesting and useful plasmonic properties. However, many outstanding issues remain to be addressed including gaining a better understanding of the intricate interaction between HGNs and cells as well as bio-accumulation and bio-clearance *in vivo*. While there has been some progress made in determining the ideal size and aspect ratio for optimal photothermal energy conversion, further research is clearly needed for a more complete understanding and full optimization. It would also be interesting to be able to determine the local temperature on the HGN surface, which is important for understanding the mechanism of cell death in photothermal therapies.

Acknowledgments

We acknowledge Ying-Chih Pu, Frank Song and Sarah Lindley for the use of some of their unpublished results on HGNs. We also acknowledge Sara Bonabi for feedback on the manuscript. We are grateful to financial support from the (ECCS-0823921) and the BES Division of the US DOE (DE-FG02-05ER46232).

References

- [1] U. Kreibig, M. Vollmer, *Optical Properties of Metal Clusters*, Springer, Berlin, 1995.
- [2] M.A. El-Sayed, *Acc. Chem. Res.* 34 (2001) 257.
- [3] S.A. Maier, H.A. Atwater, *J. Appl. Phys.* 98 (2005) 011101.
- [4] J.N. Anker, W.P. Hall, O. Lyandres, N.C. Shah, J. Zhao, R.P. Van Dyne, *Nat. Mater.* 7 (2008) 442.
- [5] P.K. Jain, X. Huang, I.H. El-Sayed, M.A. El-Sayed, *Acc. Chem. Res.* 41 (2008) 15878.
- [6] M.G. Blaber, M.D. Arnold, M.J. Ford, *J. Phys. Cond. Matter.* 22 (2010) 143201.
- [7] D.K. Gramotchev, S.I. Bozhevolnyi, *Nat. Photon.* 4 (2010) 83.
- [8] E. Prodan, C. Radloff, N.J. Halas, P. Nordlander, *Science* 302 (2003) 419.
- [9] N.J. Halas, S. Lal, W.S. Chang, S. Link, P. Nordlander, *Chem. Rev.* 111 (2011) 3913.
- [10] J.A. Schuller, E.S. Barnard, W. Cai, Y.C. Jun, J.S. White, M.L. Brogersma, *Nat. Mater.* 9 (2010) 193.
- [11] G.V.P. Kumar, *Nanophotonics* 6 (2012) 064503.
- [12] L.M. Liz-Marzan, C.J. Murphy, J. Wang, *Chem. Soc. Rev.* 43 (2014) 3820.
- [13] A.R. Melnyk, M.J. Harrison, *Phys. Rev. B* 2 (1970) 835.
- [14] S. Link, M.A. El-Sayed, *Int. Rev. Phys. Chem.* 19 (2000) 409.
- [15] M.M. Miller, A.A. Lazarides, *J. Phys. Chem. B* 109 (2005) 21556.
- [16] K.L. Kelly, E. Coronado, L.L. Zhao, G.C. Schatz, *J. Phys. Chem. B* 107 (2003) 668.
- [17] Liz-Marzan, L.M. *Materials Today Feb.* 2004 ISSN: 1369 7021.
- [18] C. Sonnichsen, T. Franzl, T. Wilk, G. von Plessen, J. Feldmann, O. Wilson, P. Mulvaney, *Phys. Rev. Lett.* 88 (2002) 077402.
- [19] A.F. Koenderink, A. Polman, *Phys. Rev. B* 74 (2006) 033402.
- [20] M.M. Miller, A.A. Lazarides, *J. Optics, A. Pure Appl. Opt.* 8 (2006) S239.
- [21] A. Feis, C. Gellini, P. Remingo-Salir, M. Becucci, *Photoacoustics* 2 (2014) 47.
- [22] M. Faraday, *Phil. Trans. R Soc. Lond.* 147 (1857) 145.
- [23] G. Mie, *Annalen der Physik* 330 (1908) 377.
- [24] A. Wokaun, J.P. Gordon, P.F. Liao, *Phys. Rev. Lett.* 48 (1982) 957.
- [25] M. Meier, A. Wokaun, *Opt. Lett.* 8 (1983) 581.
- [26] R. Graaff, J.G. Aarnoudse, J.R. Yip, P.M.A. Sloot, F.F.M. del Mul, J. Greve, M.H. Kollink, *Appl. Opt.* 31 (1992) 1370.
- [27] H. Horvath, *J. Quant. Spectrosc. Rad. Transf.* 110 (2009) 787.
- [28] Q. Fu, W. Sun, *Appl. Opt.* 40 (2001) 1354.
- [29] P. Jain, X. Huang, I.H. El-Sayed, M.A. El-Sayed, *Plasmonics* 2 (2007) 107.
- [30] N.W. Ashcroft, *Solid State Physics*, Holt Rinehart and Winston, New York, 1976.

- [31] H. Hovel, S. Fritz, A. Hilger, U. Kreibitz, M. Vollmer, *Phys. Rev. B* 48 (1993) 18178.
- [32] S. Link, M.A. El-Sayed, *Ann. Rev. Phys. Chem.* 54 (2003) 331.
- [33] K. Kolwas, A. Derkachova, *J. Quant. Spectrosc. Rad. Transf.* 114 (2013) 45.
- [34] J. Langer, S.M. Novikov, L.M. Liz-Marzan, *Nanotechnology* 26 (2015) 322001.
- [35] S. Link, M.A. El-Sayed, *J. Phys. Chem. B* 103 (1999) 4212.
- [36] C. Arbouet, D. Voisin, P. Christofilos, N. Langot, F. Del Fatti, J. Vallerr, G. Lerne, E. Celep, M. Cottancin, M. Gaudry, M. Pellarin, M. Broyer, M. Maillard, P. Pileni, M. Treguer, *Phys. Rev. Lett.* 90 (2003) 1774011.
- [37] C.L. Nehl, N.K. Grady, G.P. Goodrich, F. Tam, N.J. Halas, J.H. Hafner, *Nano Lett.* 4 (2004) 2355.
- [38] P.K. Jain, K.S. Lee, I.H. El-Sayed, M.A. El-Sayed, *J. Phys. Chem. B* 110 (2006) 7238.
- [39] L.M. Liz-Marzan, *Langmuir* 22 (2006) 32.
- [40] H. Wang, D.W. Brandl, P. Nordlander, N.J. Halas, *Acc. Chem. Res.* 40 (2007) 53.
- [41] M. Pelto, J. Aizpurua, G. Bryant, *Laser Photon. Rev.* 2 (2008) 136.
- [42] J.Z. Zhang, C. Noguez, *Plasmonics* 3 (2008) 127.
- [43] M. Grzelczak, L.M. Liz-Marzan, *Chem. Soc. Rev.* 43 (2012) 2089.
- [44] H. Xie, A. Lamour, W.E. Smith, K. Faulds, D. Graham, *J. Phys. Chem. C* 116 (2012) 8338.
- [45] A.M. Cao Jr., R. Diaz-Garcia, R. Cao, *Coord. Chem. Rev.* 253 (2009) 1262.
- [46] J.J. Mock, M. Barbic, D.R. Smith, D.A. Schultz, S. Schultz, *J. Chem. Phys.* 116 (2002) 6755.
- [47] E.A. Coronado, G.C. Shatz, *J. Chem. Phys.* 119 (2003) 3926.
- [48] C. Burda, X. Chen, R. Narayanan, M.A. El-Sayed, *Chem. Rev.* 105 (2005) 1025.
- [49] S. Eustis, M. El-Sayed, *Chem. Soc. Rev.* 35 (2006) 209.
- [50] K.S. Lee, M.A. El-Sayed, *J. Phys. Chem. B* 110 (2006) 19220.
- [51] J. Perez-Juste, I. Pastoriza-Santos, L.M. Liz-Marzan, P. Mulvaney, *Coord. Chem. Rev.* 249 (2005) 1870.
- [52] D.E. Gomez, K.C. Vernon, T.J. Davis, *Phys. Rev. B* 81 (2010) 075414.
- [53] J.Z. Zhang, *J. Phys. Chem. Lett.* 1 (2010) 686.
- [54] K.S. Lee, M.A. El-Sayed, *J. Phys. Chem. B* 109 (2005) 20331.
- [55] X. Huang, M.A. El-Sayed, *J. Adv. Res.* 1 (2010) 13.
- [56] A.M. Schwartzberg, C.D. Grant, A. Wolcott, C.E. Talley, T.R. Huser, R. Bogomolni, J.Z. Zhang, *J. Phys. Chem. B* 108 (2004) 19191.
- [57] C. Grant, T. Norman Jr., T. Morris, G. Sylwczenski, J.Z. Zhang, *SPIE Proc.* 4807 (2002) 216.
- [58] P. Albella, B. Garcia-Cueto, F. Gonzalez, F. Moreno, P.C. Wu, T.H. Kim, A. Brown, Y. Yang, H.O. Everitt, G. Videen, *Nano Lett.* 11 (2011) 3531.
- [59] C. Loo, A. Lin, L. Hirsch, M.H. Lee, J. Barton, N. Halas, J. West, R. Drezek, *Technol. Cancer Res. Treat.* 3 (2004) 33.
- [60] L.R. Hirsch, A.M. Gobin, A.R. Lowery, F. Tam, R.A. Dreyek, N.J. Halas, J.L. West, *Ann. Biomed. Eng.* 34 (2006) 15.
- [61] S. Kalele, S.W. Gosavi, J. Wiban, S.K. Kulkarni, *Curr. Sci.* 91 (2006) 1038.
- [62] J.R. Cole, N.A. Mirin, M.W. Knight, G.P. Goodrich, N.J. Halas, *J. Phys. Chem. C* 113 (2009) 12090.
- [63] C. Amiens, D. Ciuculescu-Pradines, K. Philippot, *Chem. Rev.* 308 (2016) 409.
- [64] A.M. Michaels, L. Jiang, J. Brus, *Phys. Chem. B* 104 (2000) 11965.
- [65] A.D. McFarland, M.A. Young, J.A. Dieringer, R.P. Van Duyne, *J. Phys. Chem. B* 109 (2005) 11279.
- [66] A.M. Schwartzberg, T.Y. Olson, C.E. Talley, J.Z. Zhang, *J. Phys. Chem. B* 110 (2006) 19935.
- [67] W.F. Cheong, S.A. Prael, A.J. Welch, *J. Quantum Electron.* 26 (1990) 2166.
- [68] R.W. Habash, R. Bansal, D. Krewski, H.T. Alhafid, *Crit. Rev. Biomed. Eng.* 34 (2006) 459.
- [69] K. Sokolov, M. Follen, J. Aaron, I. Pavlova, A. Malpica, R. Lotan, R. Richards-Kortum, *Cancer Res.* 63 (2003) 1999.
- [70] B.D. Chithrani, A.A. Ghazani, W.C.W. Chan, *Nano Lett.* 6 (2006) 662.
- [71] B.D. Chithrani, W.C.W. Chan, *Nano Lett.* 7 (2007) 1542.
- [72] W. Lu, C. Xiong, G. Zhang, Q. Huang, R. Zhang, C. Li, *Clin. Cancer Res.* 15 (2009) 876.
- [73] P. Douglas, R.J. Stokes, D. Graham, W.E. Smith, *Analyst* 133 (2008) 791.
- [74] E.E. Conner, J. Mwamuka, A. Gole, C.J. Murphy, M.D. Wyatt, *Small* 1 (2005) 325.
- [75] H.P. Liang, L.J. Wan, C.L. Bai, L. Jiang, *J. Phys. Chem. B* 109 (2005) 7795.
- [76] S. Preciado-Flores, D. Wang, D.A. Wheeler, R. Newhouse, J.K. Hensel, A. Schwartzberg, L. Wang, J. Zhu, M. Barboza-Flores, J.Z. Zhang, *J. Mater. Chem.* 21 (2011) 2344.
- [77] S. Adams, D. Thai, X. Mascona, A.M. Schwartzberg, J.Z. Zhang, *Chem. Mater.* 26 (2014) 6805.
- [78] M.P. Melancon, W. Lu, Z. Yang, R. Zhang, Z. Cheng, A.M. Elliot, J. Stafford, T. Olson, J.Z. Zhang, *Mol. Cancer Ther.* 7 (2008) 1730.
- [79] G.B. Braun, A. Pallaro, G. Wu, D. Missirli, J.A. Zasadzinski, M. Tirrell, N.O. Reich, *ACS Nano* 3 (2009) 2007.
- [80] J. You, R. Zhang, G. Zhang, M. Zhong, Y. Liu, C.S. Van Pelt, D. Liang, W. Wei, A.K. Sood, C. Li, *J. Cont. Release* 158 (2012) 319.
- [81] Y. Sun, Y. Xia, *Nano Lett.* 3 (2003) 1569.
- [82] E. Hao, S.Y. Li, R.C. Bailey, S.L. Zhou, G.C. Schatz, J.T. Hupp, *J. Phys. Chem. B* 108 (2004) 1224.
- [83] O. Pena, U. Pal, L. Rodriguez-Fernandez, A. Crespo-Sosa, *J. Opt. Soc. Am. B* 25 (2008) 1371.
- [84] D. Wan, H.L. Chen, Y.S. Lin, S.Y. Chuang, J. Shieh, S.H. Chen, *ACS Nano* 3 (2009) 960.
- [85] N. Del Fatti, F. Vallee, C. Flytzanis, Y. Hamanaka, A. Nakamura, *Chem Phys.* 251 (2000) 215.
- [86] J. Nappa, G. Revillod, I. Russier-Antoine, E. Benichou, C. Honin, P.F. brevet, *Phys. Rev. B* 71 (2005) 165407.
- [87] P. Mulvaney, M. Giersig, T. Ung, L.M. Liz-Marzan, *Adv. Mater.* 9 (1997) 570.
- [88] T. Ung, L.M. Liz-Marzan, P. Mulvaney, *Langmuir* 14 (1998) 3740.
- [89] R. Caruso, M. Antonietti, *Chem. Mater.* 13 (2001) 3272.
- [90] F. Caruso, R.A. Caruso, H. Mohwald, *Science* 282 (1998) 1111.
- [91] Y. Sun, B. Mayers, Y. Xia, *Nano Lett.* 2 (2002) 481.
- [92] K. An, T. Hyeon, *Nano Today* 3 (2009) 359.
- [93] S. Chah, J.H. Fendler, J. Yi, *J. Colloid Interface Sci.* 250 (2002) 142.
- [94] Z. Liang, A. Susha, F. Caruso, *Chem. Mater.* 15 (2003) 3176.
- [95] Abdolli, S. N., M. Naderi, G. Amoabediny, *Colloids Surf. A: Physicochem. Enginier Aspects* (4362013)1069.
- [96] J. Chen, B. Wiley, J. McLellan, Y. Xiong, Z.Y. Li, Y. Xia, *Nano Lett.* 5 (2005) 2058.
- [97] X. Fan, W. Zheng, D.J. Singh, *Light: Sci. Appl.* 3 (2014) e179.
- [98] E. Gonzalez, J. Arbiol, V.F. Puntes, *Science* 334 (2011) 1377.
- [99] M.R. Choi, K.J. Stanton-Maxey, J.K. Stanelin, C.S. Levin, R. Bardhan, D. Akin, S. Badve, J. Sturgis, J.P. Robinson, R. Bashir, N.J. Halas, S.E. Clare, *Nano Lett.* 7 (2007) 3759.
- [100] Z.L. Wang, T.S. Ahmad, M.A. El-Sayed, *Surface Sci.* 380 (1997) 302.
- [101] X. Hong, D. Wang, S. Cai, H. Rong, Y. Li, *JACS* 134 (2012) 18165.
- [102] B. Goris, L. Polavarapu, S. Bals, G.V. Tendeloo, L.M. Liz-Marzan, *Nano Lett.* 14 (2014) 3220.
- [103] M.H. Oh, T. Yu, S. Yu, B. Lim, K. Ko, M. Willinger, D. Seo, B. Kim, M. Cho, J. Park, K. Kang, Y. Sung, N. Pinna, T. Hyeon, *Science* 340 (2013) 964.
- [104] X. Xia, Y. Wang, A. Ruditskiy, Y. Xia, *Adv. Mater.* 25 (2013) 6313.
- [105] Kirkendall, *Trans. AIME* 171 (1947) 130.
- [106] K.N. Tu, U. Gosele, *Appl. Phys. Lett.* 86 (2005) 093111.
- [107] Y. Yin, R.M. Rioux, C.K. Erdonmez, S. Hughes, G.A. Somorjai, A.P. Alvisatos, *Science* 304 (2004) 711.
- [108] Y. Sun, Y. Xia, *Science* 298 (2002) 2176.
- [109] J. Liu, W. Bu, L. Pan, J. Shi, *Angew. Chem. Int. Ed.* 52 (2013) 4375.
- [110] I. Lisiacki, M.P. Pileni, *Langmuir* 19 (2003) 9486.
- [111] Y. Kobayashi, M. Horie, M. Konno, B. Rodriguez-Gonzalez, L.M. Liz-Marzan, *J. Phys. Chem. B* 107 (2003) 7420.
- [112] Y. Xia, Y. Xiong, B. Lim, S.E. Skrabalak, *Angew. Chem. Int. Ed. Engl.* 48 (2009) 60.
- [113] M. Grzelczak, L.M. Liz-Marzan, *Chem. Soc. Rev.* 43 (2014) 2089.
- [114] V. Salgueiriño-Maceira, M.A. Correa-Duarte, M. Farle, M.A. Lopez-Quintelz, K. Sieradzki, R. Diaz, *Langmuir* 22 (2006).
- [115] V.K. LaMer, R.H. Dinegar, *J. Am. Chem. Soc.* 72 (1950) 4847.
- [116] N.R. Jana, L. Gearheart, C.J. Murphy, *Langmuir* 17 (2001) 6782.
- [117] J. Zeng, J. Huang, W. Lu, X. Wang, B. Wang, S. Zhang, J. Hou, *Adv. Mater.* 19 (2007) 2172.
- [118] J.B. Jackson, S. Wescott, L.R. Hirsch, J.L. West, N.J. Halas, *J. Appl. Phys. Lett.* 82 (2003) 257.
- [119] C. Huang, Y. Hao, J. Nyagilo, D.P. Dave, L. Xu, X. Sun, *J. Nano Res.* 10 (2010) 137.
- [120] B.L. Sanchez-Gaytan, Z. Qian, S.P. Hastings, M.L. Rica, Z. Fakhraai, S.J. Park, *J. Phys. Chem. B* 117 (2003) 8916.
- [121] W. Shi, J. Casas, M. Venkataramasubramani, L. Tang, *ISRN Nanomater.* 2012 (2012), <http://dx.doi.org/10.5402/2012/659043> (Article ID: 659043, 9 pages).
- [122] Q. Meng, H. Li, H. Yang, *Chinese J. Chem.* 28 (2010) 2015.
- [123] X. Peng, *Metallic Nanomaterials*, vol 1, Wiley VCH Verlag Weinheim, Germany, 2009.
- [124] J. Park, J. Joo, S.G. Kwon, Y. Jang, T. Hyeon, *Angew. Chem. Int. Ed.* 46 (2007) 4643.
- [125] Y. Xiong, Q. Chen, N. Tao, J. Ye, Y. Tang, J. Feng, X. Gu, *Nanotechnology* 18 (2007) 345301.
- [126] A. Guerrero-Martinez, J. Perez-Juste, L.M. Liz-Marzan, *Adv. Mater.* 22 (2010) 1182.
- [127] J. Rodriguez-Fernandez, A.M. Funston, J. Perez-Juste, R.A. Alvarez-Puebla, L.M. Liz-Marzan, P. Mulvaney, *Phys. Chem. Chem. Phys.* 11 (2009) 5909.
- [128] Y. Bao, W. An, H. Turner, K.M. Krishnan, *Langmuir* 26 (2010) 478.
- [129] Z. Yang, N. Yang, J. Yang, J. Bergstrom, M.P. Pileni, *Adv. Funct. Mater.* 25 (2015) 891.
- [130] L.O. Svaasand, C.J. Gomer, E. Morinelli, *Laser Med. Sci.* 5 (1990) 121.
- [131] Liao, Y., A. Unterreiner, Q. Chang, N. Scherer, 105 (2001) 2135.
- [132] H. Petrova, C. Lin, S. de Liejer, M. Hu, J.M. McLellan, S.R. Siekkinen, B.J. Wiley, M. Marquez, Y. Xia, J.E. Sader, G.V. Hartland, *J. Chem. Phys.* 126 (2007) 094709.
- [133] H. Baida, P. Billaud, S. Marhaba, D. Christofilos, E. Cottancin, A. Crut, J. Lerne, P. Maioli, M. Pellarin, M. Brozer, *Nano Lett.* 9 (2009) 3463.
- [134] K.L. Knappenberger, A.M. Schwartzberg, A.M. Dowgiallo, C.A. Lowman, *J. Am. Chem. Soc.* 131 (2009) 13892.
- [135] G.V. Hartland, *Chem. Rev.* 111 (2011) 3858.
- [136] R. Newhouse, H. Wang, J.K. Hensel, D.A. Wheeler, S. Zou, J.Z. Zhang, *J. Phys. Chem. Lett.* 2 (2011) 228.
- [137] K. Kolwas, A. Derkachova, *Opt-Electr. Rev.* 18 (2010) 429.
- [138] H. Harutyunyan, A.B.F. Martinson, D. Rosenmann, L.K. Khorashad, L.V. Besterio, A.O. Govorov, G.P. Wiederrecht, *Nat. Nanotechnol.* 10 (2015) 770.
- [139] R.D. Averitt, S.L. Wescott, N.J. Halas, *Phys. Rev. B* 58 (1998) R10203R.
- [140] T.W. Roberti, B.A. Smith, Z. Zhang, *J. Chem. Phys.* 102 (1995) 3860.
- [141] A.E. Faulhaber, B.A. Smith, J.K. Anderson, J.Z. Zhang, *Mol. Cryst. Liq. Cryst.* 283 (1996) 25.
- [142] B.A. Smith, J.Z. Zhang, U. Griebel, G. Schmid, *Phys. Lett.* 270 (1997) 136.
- [143] J.H. Hodak, A. Henglein, G.V. Hartland, *J. Phys. Chem. B* 104 (2000) 9954.

- [144] S.I. Anisimov, B.L. Kapeliovich, T.L. Perel'man, *Sov. Phys.: J. Exp. Theor. Pract.* 39 (1974) 776.
- [145] S.A. Nepijko, S.A. Gorban, L.V. Viduta, R.D. Fedorovich, *Int. J. Electron.* 73 (1992) 1011.
- [146] J.H. Hodak, A. Henglein, G.V. Hartland, *J. Chem. Phys.* 111 (1999) 8613.
- [147] B.A. Smith, J.Z. Zhang, U. Griebel, G. Schmid, *Chem. Phys. Lett.* 270 (1997) 139.
- [148] M. Hu, G.V. Hartland, *J. Phys. Chem. B* 106 (2002) 7029.
- [149] A.M. Dowgiallo, K.L. Knappenberger Jr., *Phys. Chem. Chem. Phys.* 13 (2011) 21585.
- [150] S. Hashimoto, D. Werner, T. Vivada, *J. Photochem. Photobiol. C. Photochem. Rev.* 13 (2012) 28.
- [151] A.M. Dowgiallo, K.L. Knappenberger Jr., *J. Am. Chem. Soc.* 134 (2012) 19393.
- [152] J.H. Hodak, I. Martini, G.V. Hartland, *J. Phys. Chem. B* 102 (1998) 6958.
- [153] C. Voisin, N. Del Fatti, D. Christofilos, F. Vallee, *J. Phys. Chem. B* 105 (2001) 2264.
- [154] G.V. Hartland, *J. Chem. Phys.* 116 (2002) 8048.
- [155] A.M. Dowgiallo, A.M. Schwartzberg, K.L. Knappenberger Jr., *Nano Lett.* 11 (2011) 3258.
- [156] C. Guillion, P. Langot, N. Del Fatti, F. Vallee, A.S. Kirakosyan, T.V. Shahbazyan, T. Cardiani, M. Treguer, *Nano Lett.* 7 (2007) 138.
- [157] G.V. Hartland, *Annu. Rev. Phys. Chem.* 57 (2006) 403.
- [158] Lee, J.Y., M.C. Tsai, P.C. Chen, T.T. Chen, K.L. Chan, C.Y. Lee, R.K.
- [159] E. Lukianova-Hleb, Y. Hu, L. Latterini, L. Tarpani, S. Lee, R.A. Drezek, J.H. Hafner, D.O. Lapotko, *ACS Nano* 4 (2000) 2109.
- [160] L.R. Hirsch, J.B. Jackson, A. Lee, N.J. Halas, J.L. West, *Anal. Chem.* 75 (2003) 2377.
- [161] V.K. Pustovalov, A.S. Smetannikov, U.P. Zharov, *Laser Phys. Lett.* 5 (2008) 775.
- [162] A.N. Vokov, C. Sevilla, L.V. Zhigilei, *Appl. Surf. Sci.* 253 (2007) 6394.
- [163] D. Lapotko, *Int. J. Heat Mass Transf.* 52 (2009) 1540.
- [164] H.H. Richardson, Z.N. Hickman, A.O. Govorov, A.C. Thomas, W. Zhang, M.E. Kordesch, *Nano Lett.* 6 (2006) 783.
- [165] D.K. Roper, A.W. Hoepfner, *J. Phys. Chem. C* 111 (2007) 3636.
- [166] D. Lapotko, *Opt. Express* 17 (2009) 2538.
- [167] L.C. Kennedy, L.R. Bickford, N.A. Lewinski, A.J. Coughlin, Y. Hu, E.S. Day, J.L. West, R.A. Drezek, *Small* 10 (2010) 1.
- [168] I.S. Amiri, A. Nikonker, P.P. Yupapin, *Quantum Matt.* 1 (2012) 159.
- [169] R.R. Letfullin, C. Joenathan, T.F. George, V.P. Zharev, *Nanomedicine* 1 (2006) 473.
- [170] B.G. Prevo, S.A. Esakoff, A. Mikhailovsky, J.A. Zasadzinski, *Small* 4 (2008) 1183.
- [171] S.S. Chang, C.W. Shih, C.D. Chen, W.C. Lai, C.R.C. Wang, *Langmuir* 15 (1999) 701.
- [172] S. Link, M.A. El-Sayed, *J. Phys. Chem. B* 103 (1999) 8410.
- [173] S. Link, C. Burda, B. Nikoobakht, M.A. El-Sayed, *J. Phys. Chem. B* 104 (2000) 6152.
- [174] V. Kotaidis, A. Plech, *Appl. Phys. Lett.* 87 (2005) 213102.
- [175] J. Newmann, R. Brinkmann, *J. Biomed. Opt.* 10 (2005) 024001.
- [176] D.A. Wheeler, R.J. Newhouse, H. Wang, S. Zou, J.Z. Zhang, *J. Phys. Chem. C* 114 (2010) 18126.
- [177] W. Lu, G. Zhang, R. Zhang, L.G. Flores II, Q. Huang, J.G. Gelovani, C. Li, *Cancer Res.* 70 (2010) 3177.
- [178] M.C. Klein, F. Hache, D. Ricard, C. Flytzanis, *Phys. Rev. B* 42 (1990) 11123.
- [179] J.H. Hodak, A. Henglein, M. Giersig, G.V. Hartland, *J. Phys. Chem. B* 104 (2000) 9954.
- [180] M. Hu, X. Wang, G.V. Hartland, V. Salguierino-Maceira, L.M. Liz-Marzan, *Chem. Phys. Lett.* 372 (2003) 767.
- [181] C. Tabor, R. Murali, M. Mahmoud, M.A. El-Sayed, *J. Phys. Chem. A* 113 (2009) 1946.
- [182] Y. Fang, N.H. Song, D.D. Dlott, *Science* 321 (2008) 388.
- [183] G.V. Hartland, *Phys. Chem. Chem. Phys.* 6 (2004) 5263.
- [184] N. Harris, M.J. Ford, M.B. Cortie, *J. Phys. Chem. B* 110 (2006) 10701.
- [185] C.F. Bohren, D.R. Huffman, *Absorption and Scattering of Light by Small Particles*, Wiley, New York, 1998.
- [186] A.L. Gough-Palmer, W.M. Witold-Gedroyc, *World J. Gastroenterol.* 14 (2008) 7170.
- [187] Z.Z.J. Lim, J.E.J. Li, C.T. Ng, L.Y.L. Yung, B.H. Bay, *Acta. Pharmacol. Sinica* 32 (2011) 983.
- [188] J.K. Young, E.R. Figueroa, R.A. Drezek, *Annals Biomed. Eng.* 40 (2012) 48.
- [189] C. Iancu, *Biotechnol. Molecular Biol. Nanomed.* 1 (2013) 53.
- [190] D. Jaque, L. Martinez-Maestro, B. del Rosai, P. Haro-Gonzalez, A. Benayas, J.L. Plaza, E. Martin-Rodriguez, J. Garcia-Sole, *Nanoscale* 6 (2014) 9494.
- [191] R. Weissleder, *Nat. Biotechnol.* 19 (2001) 316.
- [192] X. Huang, P.K. Jain, I.H. El-Sayed, M.A. El-Sayed, *Lasers Med. Sci.* 23 (2008) 217.
- [193] V. Vongsavat, B.M. Vittur, W.W. Bryan, J.H. Kim, T.R. Lee, *ACS Appl. Mater. Interface* 3 (2011) 3616.
- [194] K.V. Maslov, V.A. Shklovski, *Sov. Phys.: J. Exper. Theor. Pract.* 4 (1957) 173.
- [195] W.C. Dewey, *Int. J. Hyperther.* 10 (1994) 457.
- [196] A.M. Elliot, J.R. Stafford, J. Schwartz, J. Wang, A.M. Shetty, C. Bourgoyne, P. O'Neal, J.D. Hazle, *Med. Phys.* 34 (2007) 3102.
- [197] E.B. Dickerson, E.C. Dreaden, X. Huang, I.H. El-Sayed, H. Chu, S. Pushpanketh, J.F. McDonald, M.A. El-Sayed, *Cancer. Lett.* 269 (2008) 57.
- [198] Hilderbrandt, B.P. Wust, O. Ahlers, A. Dieing, G. Sreenivasa, T. Kerner, R. Felix, H. Riess, *Crit. Rev. Oncol. Hemat.* 43 (2002) 33.
- [199] D.M. Simanouskii, M.A. Mackanos, A.R. Irani, C.E. O'Connell-Rodwell, C.H. Contag, H.A. Schwettman, D.V. Palankar, *Phys. Rev. E* 74 (2006) 011915.
- [200] I.H. El-Sayed, X. Huang, M.A. El-Sayed, *Cancer Lett.* 239 (2006) 129.
- [201] C.L. Chen, L.R. Kuo, C.L. Chang, Y.K. Hwu, C.K. Huang, S.Y. Lee, K. Chen, S.J. Lin, J.D. Huang, Y.Y. Chen, *Biomaterials* 31 (2010) 4104.
- [202] V.K. Pustovalov, *Chem. Phys.* 308 (2005) 103.
- [203] J.L. Roti, *Int. J. Hyperther.* 1 (2008) 3.
- [204] Y. Gu, W.R. Chen, M. Xia, S.W. Jeong, H. Liu, *Photochem. Photobiol.* 81 (2005) 1002.
- [205] T.J. Vogl, R. Straub, S. Zangos, M.G. Mack, K. Eichler, *Int. J. Hyperther.* 20 (2004) 713.
- [206] D.P. O'Neal, L.R. Hirsch, N.J. Halas, J.D. Payne, J.L. West, *Cancer Lett.* 209 (2004) 171.
- [207] X. Huang, I.H. El-Sayed, W. Qian, M.A. El-Sayed, *J. Am. Chem. Soc.* 128 (2006) 2115.
- [208] A.M. Gobin, M.H. Lee, N.J. Halas, W.D. James, R.A. Drezek, *Nano Lett.* 7 (2007) 1929.
- [209] S. Ial, S. Clare, N. Halas, *Acc. Chem. Res.* 41 (2008) 1842.
- [210] S. Lal, S.E. Clare, N.J. Halas, *Acc. Chem. Res.* 41 (2008) 1842.
- [211] W. Chen, R. Berden, M. Barteles, C. Perez-Torres, R.G. Pautler, N.J. Halas, A. Joshi, *Mol. Canc. Ther.* 9 (2010) 1028.
- [212] Y. Wang, B. Yan, L. Chen, *Chem. Rev.* 113 (2013) 1391.
- [213] D. Wu, X.D. Xu, X.J. Liu, *Solid State Commun.* 146 (2008) 7.
- [214] S. Xie, M. Jin, J. Tao, Y. Wang, Z. Xie, Y. Zhu, Y. Xia, *Chem.-A Eur. J.* 18 (2012) 14974.
- [215] C. Ayala-Orozco, C. Urban, M.W. Knight, A.S. Urban, O. Neumann, S.W. Bishnoi, S. Mukherjee, A.M. Goodman, H. Charron, T. Mitchell, M. Shea, R. Roy, S. Nanda, R. Schiff, N.J. Halas, A. Joshi, *ACS Nano* 8 (2014) 6372.
- [216] J. Chen, D. Wang, J. Xi, L. Au, A. Siekkinen, A. Warsen, Z.Y. Li, H. Zhang, Y. Xia, X. Li, *Nano Lett.* 7 (2007) 1318.
- [217] M. Hu, J.Y. Chen, Z.Y. Zi, L. Au, Y.N. Xia, *Chem. Soc. Rev.* 35 (2006) 1084.
- [218] E. Boisselier, D. Astruc, *Chem. Soc. Rev.* 38 (2009) 1759.
- [219] M.A. Bruckman, L.N. Randolph, A. Van Meter, S. Hern, A.J. Shoffstall, R.E. Taurog, N.F. Steinmetz, *Virology* 449 (2014) 163.
- [220] G. von Maltzahn, J.H. Park, A. Agrawal, N.K. Bandaru, S.K. Das, M.J. Sailor, S.N. Bhatia, *Cancer Res.* 69 (2009) 3892.
- [221] M.K. You, J. Park, S. Jon, *Theranostics* 2 (2012) 3.
- [222] S. Moreton, K. Faulds, N.C. Shand, M.A. Bedics, M.R. Detty, D. Graham, *Nanoscale* 7 (2015) 6075.
- [223] D. Schmaljohann, *Adv. Drug Deliv. Rev.* 58 (2006) 1655.
- [224] J. You, G. Zhang, C. Li, *ACS Nano* 4 (2010) 1033.
- [225] X. He, W.F. Wolkers, J.H. Crowe, D.J. Swanlund, J.C. Bischof, *Ann. Biomed. Eng.* 32 (2004) 1384.
- [226] J. Fang, H. Nakamura, H. Maeda, *Adv. Drug Deliv. Rev.* 63 (2011) 136.
- [227] B. Knoll, F. Keilmann, *Nature* 399 (1999) 134.
- [228] J. Pendry, *Science* 285 (1999) 1687.
- [229] S.S. Davis, *Adv. Drug Deliv. Rev.* 56 (2004) 1241.
- [230] R. Kumar, A.N. Maitra, P.K. Patanjali, P. Sharma, *Biomaterials* 26 (2005) 6743.
- [231] S.M. Lee, H. Chen, C.M. Dettmer, T.V. O'Halloran, S.T. Nguyen, *J. Amer. Chem. Soc.* 129 (2007) 15096.
- [232] J.X. Liu, H.Y. Su, D.P. Sun, B.Y. Zhang, W.X. Li, *J. Am. Chem. Soc.* 135 (2013) 16284.
- [233] M.C. Woodle, M.S. Newman, F.J. Martin, *Int. J. Pharm.* 88 (1992) 327.
- [234] J. Meyer, D. Whitcomb, D. Collins, *Biochem. Biophys. Res. Commun.* 199 (1994) 433.
- [235] K. Rittner, A. Benavente, A. Bompard-Sorlet, F. Heitz, G. Divita, R. Brasseur, E. Jacobs, *Mol. Ther.* 5 (2002) 104.
- [236] F. Novio, J. Simmchen, N. Vazquez-Mera, L. Amorin-Ferre, D. Ruiz-Molina, *Coord. Chem. Rev.* 257 (2013) 2839.
- [237] C. Boyer, J.A. Zasadzinski, *ACS Nano* 1 (2007) 176.
- [238] J. You, R. Zheng, C. Xiong, M. Zhong, M. Melancon, S. Gupta, A.M. Nick, A.K. Sood, C. Li, *Cancer Res.* 72 (2012) 4777.
- [239] S. Gupta, J. Stafford, S. Javadi, E. Ozkan, J.E. Ensor, K.C. Wright, A.M. Elliot, Y. Jian, R.E. Serda, K.A. Dixon, J.J. Miller, S. Klump, M.J. Wallace, C. Li, *J. Vasc. Interv. Radiol.* 23 (2012) 553.
- [240] S. Loo, J. Rine, *Annu. Rev. Cell Dev. Biol.* 11 (1995) 519.
- [241] S.M. Elbasher, J. Harborth, W. Lendeckel, A. Yalcin, K. Weber, T. Tuschi, *Nature* 411 (2001) 494.
- [242] M.T. McManus, P.A. Sharp, *Nat. Rev. Genet.* 3 (2002) 737.
- [243] C.C. Chen, Y.P. Lin, C.W. Wang, *J. Am. Chem. Soc.* 128 (2006) 3709.
- [244] M.D. Shahbazian, M. Grunstein, *Annu. Rev. Biochem.* 76 (2007) 75.
- [245] R. Huschka, A. Barhoumi, Q. Liu, J.A. Roth, L. Ji, N.J. Halas, *ACS Nano* 6 (2012) 7681.
- [246] H. Kim, W.J. Kin, *Small* 10 (2014) 117.
- [247] M.K. Yu, J. Park, S. Jon, *Theranostics* 2 (2012) 3.
- [248] R.K. Visaria, R.J. Griffin, B.W. Williams, E.S. Ebbini, G.F. Paciotti, C.W. Song, J.C. Bischof, *Mol. Cancer Ther.* 5 (2006) 1014.
- [249] P.S. Ghosh, C.K. Kim, G. Han, N.S. Forbes, V.M. Rotello, *ACS Nano* 2 (2008) 2213.
- [250] A. Elbakry, A. Zaky, R. Liebl, R. Rachel, A. Goepferich, M. Breunig, *Nano Lett.* 9 (2009) 2059.
- [251] J.S. Lee, J.J. Green, K.T. Love, J. Sunshine, R. Langer, D.G. Anderson, *Nano Lett.* 9 (2009) 2402.
- [252] P.A. Wender, J.B. Rothbard, T.C. Jessop, E.L. Kreider, B.L. Wylie, *J. Am. Chem. Soc.* 124 (2002) 13382.
- [253] V.P. Tochilin, *Adv. Drug Deliv. Rev.* 60 (2008) 548.
- [254] B. Radt, T.A. Smith, F. Carvso, *Adv. Mater.* 16 (2004) 2184.
- [255] A.P. Goodwin, J.L. Mynar, Y. Ma, G.R. Fleming, J.M.J. Frechet, *J. Am. Chem. Soc.* 127 (2005) 9952.
- [256] M. Das, N. Sanson, D. Fava, E. Kumacheva, *Langmuir* 23 (2007) 196.
- [257] G. Wu, A. Mikhailovsky, H.A. Khant, C. Fu, W. Chiu, J.A. Zasadzinski, *J. Am. Chem. Soc.* 130 (2008) 8175.

- [258] J. Chen, F. Saeki, B.J. Wiley, H. Cang, M.J. Cobb, Z.Y. Li, L. Au, H. Zhang, M.B. Kimmey-Xingde, Y. Xia, *Nano Lett.* 5 (2005) 473.
- [259] E. Wijaya, C. Lenaerts, S. Maricot, J. Hastanin, J.P. Vilcot, R. Boukherroub, S. Szunerits, *Curr. Opin. Solid State Mater. Sci.* 15 (2011) 208.
- [260] H. Takahashi, Y. Nildom, S. Yamada, *Chem. Commun.* (2005) 2247.
- [261] P. Jain, S.L. Kyeong, I.H. El-Sayed, M.A. El-Sayed, *J. Phys. Chem. B* 110 (2006) 7238.
- [262] M.G. Albrecht, J.A. Creighton, *J. Am. Chem. Soc.* 99 (1977) 5215.
- [263] D.L. Jeanmaire, R.P. Van Duyne, *J. Electr. Chem.* 84 (1977) 1.
- [264] M. Moskovits, *J. Chem. Phys.* 69 (1978) 4159.
- [265] C.G. Blatchford, J.R. Campbell, J.A. Creighton, *Surface Sci.* 120 (1982) 435.
- [266] A. Otto, I. Mroczek, H. Grabhorn, W.A. Kemann, *J. Phys. Condens. Mater.* 4 (1992) 1143.
- [267] A. Campion, P. Kambhampati, *Chem. Soc. Rev.* 27 (1998) 241.
- [268] K.H. Kneipp, I. Kneipp, I. Itzkan, R.R. Dasari, M.S. Feld, *J. Condens. Mater.* 14 (2002) R597.
- [269] B. Nikoobakht, *J. Phys. Chem. A* 107 (2003) 3372.
- [270] P.L. Stiles, J.A. Dieringer, N.C. Shah, R.P. Van Duyne, *Ann. Rev. Anal. Chem.* 1 (2008) 601.
- [271] M. Fan, G.F.S. Andrade, A.G. Brolo, *Analyt. Chim. Acta* 693 (2011) 7.
- [272] M. Vendrell, K.K. Marti, K. Dhaliwal, Y.T. Chang, *Trends Biotechnol.* 31 (2013) 249.
- [273] M. Moskovits, *Rev. Mod. Phys.* 57 (1985) 783.
- [274] S. Nie, S.R. Emory, *Science* 275 (1997) 1102.
- [275] K.B. Jian, M. Maillared, L. Brus, *J. Phys. Chem. B* 107 (2003) 9964.
- [276] A. Schwartzberg, J.Z. Zhang, *J. Phys. Chem. C* 112 (2008) 10323.
- [277] J.A. Creighton, C.G. Blatchford, M.G. Albrecht, *J. Chem. Soc. Faraday Trans. 2* (75) (1979) 790.
- [278] K. Kneipp, H. Kneipp, R. Manshara, E.B. Hanlon, I. Itzkan, R.R. Dasari, M.S. Feld, *Appl. Spectrosc.* 52 (1998) 1493.
- [279] M. Kahraman, M.M. Yazici, F. Sahin, O.F. Bayrak, M. Culha, *Appl. Spectrosc.* 61 (2007) 479.
- [280] K.G. Stamplecoski, J.C. Scaiano, *J. Phys. Chem. C* 115 (2011) 1403.
- [281] B. Sharma, R.R. Frontiera, A.I. Henry, E. Ringe, R.P. Van Duyne, *Mater. Today* 15 (2012) 16.
- [282] K. Kneipp, H. Kneipp, J. Kneipp, *Acc. Chem. Res.* 39 (2006) 443.
- [283] S. Lee, S. Kim, J. Choo, S.Y. Shin, Y.H. Lee, H.Y. Choi, S. Ha, K. Kang, C.H. Oh, *Anal. Chem. Res.* 79 (2007) 916.
- [284] X. Qian, X.H. Peng, D.O. Ansari, Q. Yin-Goen, G.Z. Chen, D.M. Shin, L. Yang, A.N. Young, M.D. Wang, S. Nie, *Nat. Biotechnol.* 26 (2008) 83.
- [285] L. Rivas, S. Sanchez-Cortes, J.V. Garcia-Ramos, G. Morcillo, *Langmuir* 16 (2000) 9722.
- [286] V.S. Tiwari, T. Oleg, G.K. Darbha, W. Hardy, J.P. Singh, P.C. Ray, *Chem. Phys. Lett.* 444 (2007) 77.
- [287] S. Lee, H. Chon, M. Lee, J. Choo, S.Y. Shin, Y.H. Lee, I.J. Rhyu, S.W. Son, C.H. Oh, *Biosens. Bioelectr.* 24 (2009) 2260.
- [288] M. Quinten, *J. Clust. Sci.* 10 (1999) 319.
- [289] I. Montes-Burgos, D. Walezk, P. Hole, J. Smith, I. Lynch, K. Dawson, *J. Nanopart. Res.* 12 (2010) 47.
- [290] A.M. Schwartzberg, T.Y. Oshiro, J.Z. Zhang, T. Huser, C.E. Talley, *Anal. Chem.* 78 (2006) 4732.
- [291] T.A. Laurence, G. Braun, C. Talley, A. Schwartzberg, M. Moskovits, N. Reich, T. Huser, *J. Am. Chem. Soc.* 131 (2008) 162.
- [292] B. Cox, J.G. Lauffer, S.R. Arridge, P.C. Beard, *J. Biomed. Opt.* 6 (2012) 061202.
- [293] G.J. Ashwell, P. Leeson, G.S. Bhatta, C.R. Brown, *J. Opt. Soc. Am. B* 15 (1998) 484.
- [294] P. Galletto, H.H. Girault, C. Gomis-Bas, D.J. Schriffin, R. Antoine, M. Broyer, P.F. Brevet, *J. Phys. Condens. Mater.* 19 (2007) 375108.
- [295] C.K. Chen, A.R.B. de Castro, Y.R. Shen, *Phys. Rev. Lett.* 46 (1981) 2.
- [296] O. Perez-Gonzalez, N. Zabala, A.G. Borisov, N.J. Halas, P. Nordlander, J. Aizpuru, *Nano Lett.* 10 (2010) 3090.
- [297] L.S. Slaughter, Y. Wu, B.A. Willingham, P. Nordlander, S. Link, *ACS Nano* 4 (2010) 4657.
- [298] P. Song, P. Nordlander, S. Gao, *J. Chem. Phys.* 134 (2011) 074701.
- [299] L. Gunnarso, T. Rindzevicius, J. Prinkulis, B. Kasemo, M. Kall, S. Zhou, G.C. Schatz, *J. Phys. Chem. B* 109 (2005) 1079.
- [300] P.J. Shuck, D.F. Fromm, A. Sundaramurthy, G.S. Kino, W.E. Moerner, *Phys. Rev. Lett.* 94 (2005) 1079.
- [301] I. Romero, J. Aizpuru, G.W. Bryant, F.J. Garcia de Abajo, *J. Opt. Express* 14 (2006) 9988.
- [302] H. Xu, E.J. Bjerneld, M. Kall, L. Borjesson, *Phys. Rev. Lett.* 83 (1999) 4357.
- [303] M. Chandra, A.M. Dowgiallo, K.L. Knappenberger Jr., *J. Am. Chem. Soc.* 132 (2010) 15782.
- [304] S.M. Stagg, K.L. Knappenberger Jr., A.M. Dowgiallo, M. Chandra, *J. Phys. Chem. Lett.* 2 (2011) 2946.
- [305] M.A. Mahmoud, M.A. El-Sayed, *J. Phys. Chem. C* 114 (2010) 7436.
- [306] M. Chandra, A.M. Dowgiallo, K.L. Knappenberger Jr., *J. Phys. Chem. C* 114 (2010) 19971.
- [307] J. Tiggesbaumer, L. Koller, K.H. Meiwes-Broer, A. Liesch, *Phys. Rev. A* 48 (1993) 1749.
- [308] E. Prodan, P. Nordlander, *Chem. Phys.* 120 (2004) 5444.
- [309] J. Nappa, I. Russier-Antoine, E. Benichou, C. Jonin, P.F. Brevet, *J. Chem. Phys.* 125 (2006) 184712.
- [310] I. Russier-Antoine, E. Benichou, G. Bachelier, C. Jonin, P.F. Brevet, *J. Phys. Chem. C* 111 (2007) 9044.
- [311] R. Acevedo, R. Lombardini, N.J. Halas, *J. Phys. Chem. A* 113 (2009) 13173.
- [312] W.E. Doering, S. Nie, *Anal. Chem.* 75 (2003) 6171.
- [313] R.A. Alvarez-Puebla, L.M. Liz-Marzan, *Small* 6 (2010) 604.
- [314] B. Guven, N. Basaran-Akqui, E. Temur, U. Tamer, I.H. Boyaci, *Analyst* 136 (2011) 740.
- [315] G. Sabatte, R. Keir, M. Lawlor, M. Black, D. Graham, W.E. Smith, *Anal. Chem.* 80 (2008) 2351.
- [316] C. Song, Z. Wang, R. Zhang, J. Yang, X. Tan, Y. Cui, *Biosens. Bioelectr.* 25 (2009) 826.
- [317] Y. Wang, L. Chen, *Nanomed. Nanotechnol. Biol. Med.* 7 (2011) 385.
- [318] K. Kneipp, Y. Wang, H. Kneipp, L.T. Perelman, I. Itzkan, R.R. Dasari, M.S. Feld, *Phys. Rev. Lett.* 78 (1997) 1667.
- [319] A.W. Peterson, R.J. Heaton, R. Georgiadis, *J. Am. Chem. Soc.* 122 (2000) 7837.
- [320] M. Bally, M. Halter, J. Voros, H.M. Grandin, *Surf. Interface Anal.* 38 (2006) 1442.
- [321] G. Wang, H.Y. Park, R.J. Lipert, *Anal. Chem.* 81 (2009) 9643.
- [322] L. Rodriguez-Lorenzo, L. Fabris, R.A. Alvarez-Perez, *Analyt. Chim. Acta* 745 (2012) 10.
- [323] L.J. Kricka, *Clin. Chem.* 38 (1992) 327.
- [324] W.C. Chan, D.J. Maxwell, X. Gao, R.E. Bailey, M. Han, S. Nie, *Curr. Opin. Biotechnol.* 13 (2002) 40.
- [325] H. Chon, S. Lee, S.W. Son, C.H. Oh, J. Choo, *Anal. Chem.* 81 (2009) 3029.
- [326] H. Chon, S. Lee, S.Y. Yoon, S.I. Chang, D.W. Lim, J. Choo, *Chem. Commun.* 47 (2011) 12515.
- [327] R. Anderson, J.A. Parush, *J. Invest. Dermatol.* 77 (1981) 13.
- [328] J.M. Schmitt, A. Knuttel, M. Yadlowsky, M.A. Eckhaus, *Phys. Med. Biol.* 39 (1994) 1705.
- [329] C.K. Sun, C.C. Chen, S.W. Chen, T.H. Tsai, Y.C. Chen, B.L. Lin, *Opt. Lett.* 28 (2003) 2488.
- [330] A.N. Bashkatov, E.A. Genina, V.I. Kochubey, V.V. Tuchin, *J. Phys. D. Appl. Phys.* 38 (2005) 2543.
- [331] M. Balu, T. Baldacchini, J. Carter, T.B. Karasieva, R. Zadayan, B.J. Tromberg, *J. Biomed. Opt.* 14 (2009) 010508.
- [332] D. Kobat, M.E. Durst, N. Nishimura, A.W. Wong, C.B. Schaffer, C. Xu, *Opt. Express* 17 (2009) 13354.
- [333] M.A. Bedics, H. Kearns, J.M. Cox, S. Mabbott, F. Ali, N.C. Shand, K. Faulds, J.B. Benedict, D. Graham, M.R. Dettly, *Chem. Sci.* 6 (2015) 2302.
- [334] C.G.A. Hoelen, F.F.M. de Mul, R. Pongers, A. Dekker, *Opt. Lett.* 23 (1998) 648.
- [335] V. Ntziachristos, *Nat. Methods* 7 (2010) 603.
- [336] R. Weissleder, *Nat. Rev. Cancer* 2 (2002) 11.
- [337] X.D. Wang, Y.J. Pang, G. Ku, X.Y. Xie, G. Stoica, L.H.V. Wang, *Nat. Biotechnol.* 21 (2003) 80034.
- [338] S.A. Ermilov, T. Khampirad, A. Conjusteau, M.H. Leonard, R. Laceywell, K. Menta, *J. Biomed. Opt.* 14 (2009) 024007.
- [339] Y.S. Chen, W. Frey, S. Kim, K. Homan, P. Kruizinga, K. Sokolov, S. Emelianov, *Opt. Express* 18 (2010) 8867.
- [340] X. He, K. Wang, Z. Cheng, *Nat. Biotechnol.* 22 (2006) 339.
- [341] P. Debbage, W. Jäschke, *Hist. Chem. Cell Biol.* 130 (2008) 845.
- [342] E. Altinoglu, J.H. Adair, *Nanomed. Nanobiotechnol.* 2 (2010) 461.
- [343] B. Blasiak, F.C.J.M. Van Veggel, B. Tomanek, *J. Nanomater.* (2013) (Article ID 148578).
- [344] M. Bruchez Jr., M. Moronne, P. Gin, S. Weiss, A.P. Alivisatos, *Science* 281 (1998) 2013.
- [345] I.L. Medintz, H.T. Uyeda, E.R. Goldman, H. Mattoussi, *Nat. Mater.* 4 (2005) 435.
- [346] A. Fernandez-Suarez, Y. Ting, *Nat. Rev. Mol. Cell Biol.* 9 (2008) 929.
- [347] C.J. Xu, G.A. Tung, S.H. Sun, *Chem. Mater.* 20 (2008) 4167.
- [348] J. Li, H. Li, K. Wang, X. Zhang, C. Yao, Y. Zhang, P. Yuan, *Opt. Express* 21 (2013) 21414.
- [349] E. Petryayera, W.R. Algar, I.L. Medintz, *Appl. Spectrosc.* 67 (2013) 215.
- [350] J. Yguerabide, E.E. Yguerabide, *Anal. Biochem.* 262 (1998) 137.
- [351] N.C. Shaner, P.A. Steinbach, R.Y. Tsien, *Nat. Methods* 2 (2005) 905.
- [352] A. Elsaesser, C.V. Howard, *Adv. Drug Deliv. Rev.* 64 (2012) 129.
- [353] N.V. Gopee, D.W. Roberts, P. Webb, C.R. Cozart, P.H. Sitonen, A.R. Warbitton, W.W. Yu, V.L. Colvin, N.J. Walker, P.C. Howard, *Toxicol. Sci.* 98 (2007) 249.
- [354] B.P. Jackson, D. Bugge, J.F. Ranville, C.Y. Chen, *Environ. Sci. Technol.* 46 (2012) 5550.
- [355] A. Bruneau, M. Fortier, F. Gagne, C. Gagnon, P. Turcotte, A. Tayabal, T.L. Davis, M. Auffret, M. Fournier, *Environ. Sci. Process. Impacts* 15 (2013) 596.
- [356] D. Kim, S. Park, J.H. Lee, Y.Y. Jeong, S. Jon, *J. Am. Chem. Soc.* 129 (2007) 7661.
- [357] J.J. Pasternak, E.E. Williamson, *Mayo Clin. Proc.* 87 (2012) 390.
- [358] M. Attia, N. Anton, R. Akasov, M. Chipper, E. Markvicheva, T.F. Vandanme, *Pharm. Res.* (2015) 1.
- [359] M. Eghtedari, A. Oraevsky, J.A. Copeland, N.A. Kotov, A. Conjusteau, M. Motamedi, *Nano Lett.* 7 (2007) 1914.
- [360] H. Chen, Z. Sun, W. Ni, K.C. Woo, H.Q. Lin, L. Song, C. Yan, J. Wang, *Small* 5 (2009) 2111.
- [361] E. Boote, G. Fent, V. Kattumuri, S. Casteel, K. Katti, N. Chandra, R. Kannan, K. Katti, R. Churchill, *Acad. Radiol.* 17 (2010) 410.
- [362] N. Khlebtsov, L. Dykman, *Chem. Soc. Rev.* 40 (2011) 1647.
- [363] C. Alric, J. Taleb, G. Le Duc, C. Mandon, A.C. Le Meur-Herland, T. Brochard, F. Vocanson, M. Janier, P. Perrieat, S. Roux, O. Tillement, *J. Am. Chem. Soc.* 130 (2008) 5908.
- [364] S. Ahn, S.Y. Jung, S.J. Lee, *Molecules* 18 (2003) 5858.
- [365] A.M. Alkhalany, C.J. Murphy, *J. Nanopart. Res.* 12 (2010) 2313.
- [366] Q. Zhang, N. Iwakuma, P. Sharma, B.M. Moudgil, C. Wu, J. McNeill, H. Jiang, S.R. Grobmyer, *Nanotechnology* 20 (2009) 395102.
- [367] Y. Sun, B. Mayers, Y. Xia, *Adv. Mater.* 15 (2003) 641.
- [368] V. Pansare, S. Hejazi, R.K. Prudhomme, *ACS Chem. Mater.* 24 (2012) 812.

- [369] J. Sun, E.M. Goldys, *J. Phys. Chem. C* 112 (2008) 9261.
- [370] M. Xu, L.V. Wang, *Rev. Sci. Instr.* 77 (2006) 041101.
- [371] W. Li, X. Chen, *Nanomedicine* 10 (2015) 299.
- [372] P.J. Van de Berg, K. Daoudi, W. Stenberger, *Photoacoustics* 3 (2015) 89.
- [373] X. Liang, Z. Deng, L. Jing, X. Li, Z. Dai, C. Li, M. Huang, *Chem. Commun.* 94 (2013) 11029.
- [374] G. Balasundaram, C.J.H. Ho, K. Li, W. Driessen, U.S. Dinish, C.L. Wong, V. Ntziachristos, B. Li, M. Olivo, *Int. J. Nanomed.* 10 (2015) 387.
- [375] U.S. Dinish, Z. Song, C. Ju, H. Ho, G. Balasundaram, A.B.E. Attia, X. Lu, B.Z. Tang, B. Liu, M. Olivo, *Adv. Funct. Mater.* 25 (2015) 2316.
- [376] E. Carlson, G. Perez-Abadia, S. Adams, J.J. Zhang, K.A. Kang, C. Maldonado, *J. Acupunct. Meridian Stud.* (2015), in press.